To cite this document:
D. Liu, B. Lecampion "Propagation of a plane-strain hydraulic fracture accounting for a rough cohesive zone" *J. Mech. Phys. Sol.* (2021)
(received Nov. 24, 2020 , accepted Jan. 14, 2021)
https://doi.org/10.1016/j.jmps.2021.104322

Propagation of a plane-strain hydraulic fracture accounting for a rough cohesive zone

Dong Liu[a], Brice Lecampion[a,]

[a] *Geo-Energy Laboratory-Gaznat Chair on Geo-Energy, Ecole Polytechique Fédérale de Lausanne, EPFL-ENAC-IIC-GEL, Lausanne CH-1015, Switzerland*

Abstract

The quasi-brittle nature of rocks challenges the basic assumptions of linear hydraulic fracture mechanics (LHFM): namely, linear elastic fracture mechanics and smooth parallel plates lubrication fluid flow inside the propagating fracture. We relax these hypotheses and investigate in details the growth of a plane-strain hydraulic fracture in an impermeable medium accounting for a rough cohesive zone and a fluid lag. In addition to a dimensionless toughness and the time-scale t_{om} of coalescence of the fluid and fracture fronts governing the fracture evolution in the LHFM case, the solution now also depends on the ratio between the in-situ **stress** and material peak cohesive stress σ_o/σ_c and the intensity of the flow deviation induced by aperture roughness (captured by a dimensionless power exponent). We show that the solution is appropriately described by a nucleation time-scale $t_{cm} = t_{om} \times (\sigma_o/\sigma_c)^3$, which delineates the fracture growth into three distinct stages: a nucleation phase ($t \ll t_{cm}$), an intermediate stage ($t \sim t_{cm}$) and late time ($t \gg t_{cm}$) stage where convergence toward LHFM predictions finally occurs. A highly non-linear hydro-mechanical coupling takes place as the fluid front enters the rough cohesive zone which itself evolves during the nucleation and intermediate stages of growth. This coupling leads to significant additional viscous flow dissipation. As a result, the fracture evolution deviates from LHFM predictions with shorter fracture lengths, larger widths and net pressures. These deviations from LHFM ultimately decrease at late times ($t \gg t_{cm}$) as the ratios of the lag and cohesive zone sizes with the fracture length both become smaller. The deviations increase with larger dimensionless toughness and larger σ_o/σ_c ratio, as both have the effect of further localizing viscous dissipation near the fluid front located in the small rough cohesive zone. The convergence toward LHFM can occur at very late time compared to the nucleation time-scale t_{cm} (by a factor of hundred to thousand times) for realistic values of σ_o/σ_c encountered at depth. The impact of a rough cohesive zone appears to be prominent for laboratory experiments and short in-situ injections in quasi-brittle rocks with ultimately a larger energy demand compared to LHFM predictions.

Keywords: Fluid-driven fractures, Fracture process zone, Cohesive zone model, Fluid flow in rough fractures, Fluid lag

1. Introduction

The growth of a hydraulic fracture (HF) in an impermeable linear elastic solid is now relatively well understood, in particular the competition between the energy dissipated in the creation of new fracture surfaces and the one dissipated in viscous fluid flow. Such a competition leads to distinct propagation regimes depending on the main dissipative mechanism (Detournay, 2016). Linear elastic fracture mechanics (LEFM) combined with lubrication theory (linear hydraulic fracture mechanics - LHFM for short) have successfully predicted experimental observations for the growth of a simple planar fracture in model materials such as PMMA and glass (Bunger & Detournay, 2008; Lecampion et al., 2017; Xing et al., 2017). However, some observations on rocks at the laboratory (Thallak et al., 1993; Van Dam & de Pater, 1999) and field scales (Shlyapobersky, 1985; Shlyapobersky et al., 1988) are not consistent, and some indicate that linear hydraulic fracture mechanics (LHFM) underestimates the observed fluid pressure and overestimates the fracture length. These observations hint toward a possibly larger energy demand compared to LHFM predictions and challenge two of its basic assumptions: i) fracture process governed by LEFM and ii) lubrication flow between two smooth parallel surfaces resulting in Poiseuille's law. A non-linear process zone always exists in the vicinity of the fracture tip (Fig. 1). This is especially true for quasi-brittle materials like rocks. The stresses are capped by a finite peak strength in the fracture process zone while the aperture roughness is no longer negligible and decreases the fracture permeability. How such non-linearities affect the solid-fluid coupling inside the fracture and as a result its growth is the main goal of this paper. We focus on the propagation of a plane-

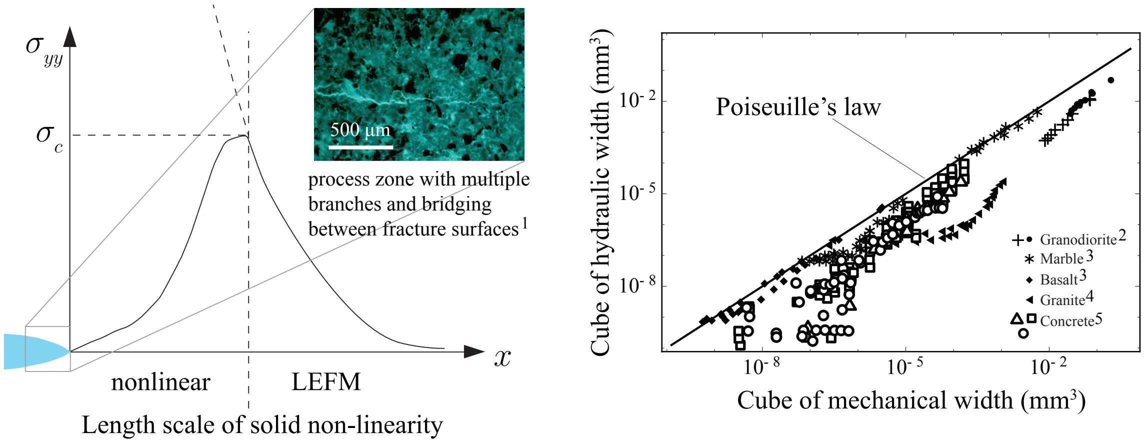

a) b)

Figure 1: Illustration of a) the length scale of solid non-linearity and b) deviated fluid flow from Poiseuille's law (cubic law). Figure b) is adapted from figure 5 in Renshaw (1995) with additional data. The superscripts indicate the source of the image in figure a) 1. Lhomme (2005), and the source of the data in figure b): 2. Schrauf & Evans (1986); 3. Witherspoon et al. (1980); 4. Raven & Gale (1985); 5. Garagash (2015); Breysse & Gérard (1997).

strain hydraulic fracture from nucleation to the late stages of growth where the process zone is inherently much smaller than the fracture length.

A number of previous investigations have dealt with the relaxation of the LEFM assumption on HF growth: either using theories accounting for bulk plastic dissipation around the tip (Papanastasiou, 1997, 1999; Papanastasiou & Atkinson, 2006; Sarris & Papanastasiou, 2013), or with an increasing apparent fracture toughness with length embedding different toughening mechanisms (Liu et al., 2019), or/and adopting cohesive zone models (CZM) as a propagation criterion (see Lecampion et al. (2018) for review). Among these approaches, cohesive zone models are the most widely used due to their simplicity: the fracture growth is simply tracked via a cohesive traction-separation law. Studies of hydraulically driven fracture using CZM (Chen et al., 2009; Chen, 2012; Lecampion, 2012; Yao et al., 2015) all show that the numerical solutions can be well approximated with LEFM/LHFM solutions. However these conclusions just follow from the fact that these simulations fall in the small-scale-yielding limit where the cohesive zone only takes up a small fraction of the whole fracture. In addition, in all these contributions, the existence of a fluid lag is neglected as well as the effect of roughness on flow. The assumption of a negligible fluid lag is often claimed to be valid for sufficiently deep fractures (where the confining stress is large) on the basis of the LHFM results.

However, the existence of a fluid lag is to lubrication flow what the process zone is to fracture mechanics. It removes the negative fluid pressure singularities at the fracture tip associated with suction resulting from the elasto-hydrodynamics coupling (Desroches et al., 1994; Garagash & Detournay, 2000). In fact, the presence of a fluid lag is necessary if accounting for the presence of a cohesive zone in order to ensure that the stresses remain finite. Rubin (1993) has pioneered studies accounting for a cohesive zone and a fluid lag by investigating the stress field around a plane-strain HF. The obtained results are, however, restricted to the particular case where the fluid lag is always larger than the cohesive zone. Rubin (1993) argues that the fluid lag increases with the fracture length and thus possibly influences the off-plane inelastic deformation. Recently, Garagash (2019) has derived the complete solution of a steadily moving semi-infinite smooth cohesive fracture with a fluid lag. The results demonstrate the strong influence of the ratio between the minimum in-situ compressive stress and the material peak cohesive stress σ_o/σ_c on the near tip asymptotes. Such a semi-infinite fracture solution is obviously valid only when the process zone has fully nucleated and is smaller than the fracture length. These investigations assume smooth fracture surfaces in the cohesive zone (and thus Poiseuille's law). The effect of roughness on the interplay between the fluid front and cohesive zone growth still calls for further investigation.

In this paper, we investigate the growth of a finite plane-strain hydraulic fracture from nucleation to the late stage of growth accounting for the presence of both a cohesive zone and a fluid lag. We also investigate the impact of a decreased hydraulic conductivity in the rough cohesive zone using existing phenomenological approximations. After a description of the model, we discuss the overall structure of the solution thanks to a scaling analysis. We then explore the coupled effect of the fluid lag, cohesive zone and roughness numerically using a specifically developed numerical scheme. We then discuss implications for the HF growth both at the laboratory and field scales.

2. Problem Formulation

We consider a plane-strain hydraulic fracture of half-length ℓ propagating in an infinite homogeneous impermeable quasi-brittle isotropic medium (Fig. 2). We denote σ_o as the minimum in-situ compressive stress acting normal to the fracture plane. The fracture growth occurs in pure tensile mode and is driven by the injection of an incompressible Newtonian fluid at a constant rate Q_o in the fracture center. We account for both the existence of a cohesive zone (of length ℓ_{coh}) and a fluid-less cavity (of length $\ell - \ell_f$) near the tips of the propagating fracture as described in Fig. 2.

2.1. Solid mechanics

2.1.1. Cohesive zone model

We adopt for simplicity a linear-softening cohesive zone model to simulate the fracture process zone, where cohesive traction decreases linearly at the tip from the peak cohesive stress σ_c to zero at a critical aperture w_c, as illustrated in Fig. 2. Such a traction separation law can be simply written as:

$$\sigma_{coh}(w) = \begin{cases} \sigma_c(1 - w_c) & 0 \leq w < w_c \\ 0 \quad w > w_c \end{cases} \tag{1}$$

where σ_c is the material peak strength (the maximum cohesive traction). The length of the cohesive zone ℓ_{coh} is given by the distance from the fracture tip where the critical opening is reached: $w(\ell_{coh}) = w_c$. For such a linear weakening model, the fracture energy is given by:

$$G_c = \frac{1}{2}\sigma_c w_c \tag{2}$$

Note that in linear elastic fracture mechanics in pure mode I, the fracture energy is related to the material fracture toughness K_{Ic} by Irwin's relation for co-planar growth $G_c^{LEFM} = K_{Ic}^2/E'$, where E' is the plane-strain elastic modulus. Equalizing the quasi-brittle fracture energy with the LEFM expression allows to define an equivalent fracture toughness

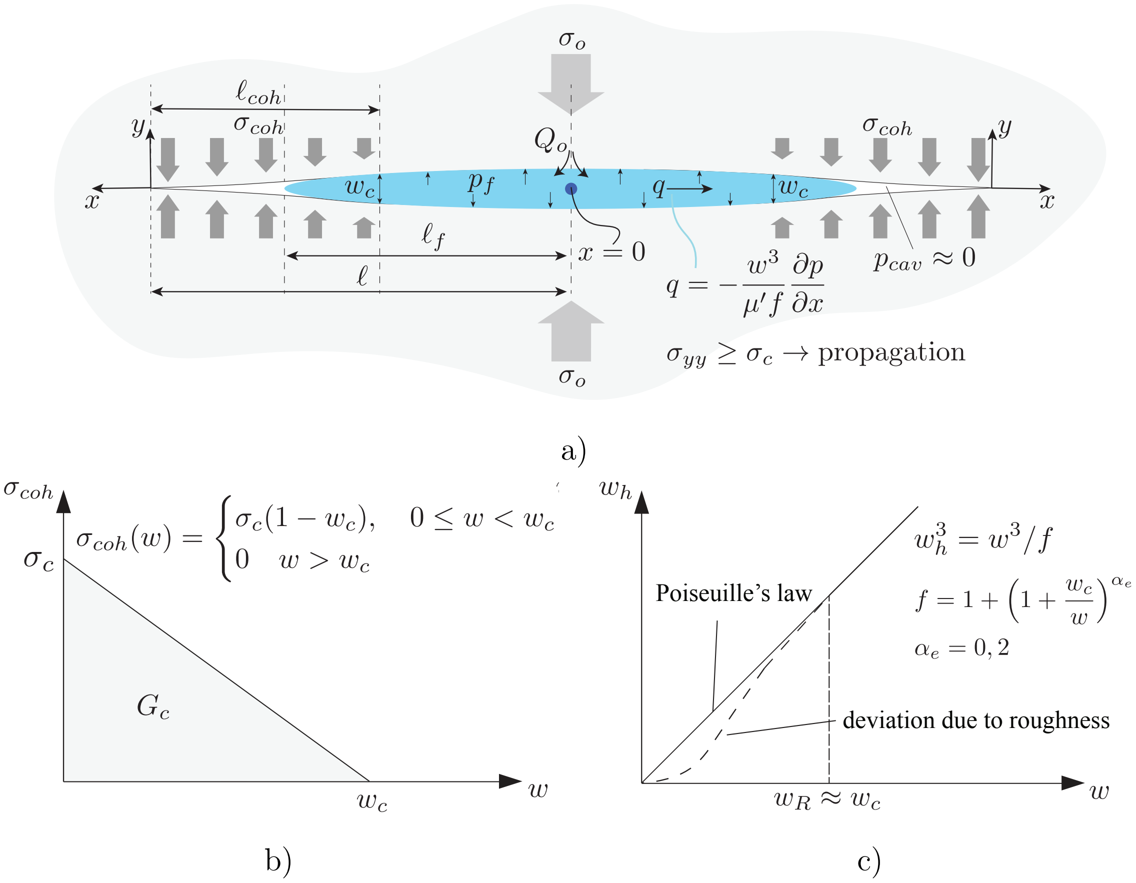

Figure 2: Illustration of a) a propagating plane-strain hydraulic fracture accounting for a cohesive zone and a fluid lag, b) a linear softening cohesive zone model, and c) roughness-induced deviation of the fluid flow inside the cohesive zone.

$K_{Ic} = \sqrt{G_c E'}$ thus allowing comparison with known results for HF growth under the LEFM assumption.

2.1.2. Elastic deformation

For a purely tensile plane-strain fracture, in an infinite elastic medium, the quasi-static balance of momentum reduces to the following boundary integral equation (see for example Hills et al. (1996)):

$$\frac{E'}{4\pi}\int_{-\ell}^{\ell}\frac{\partial w(x',t)}{\partial x'}\frac{\mathrm{d}x'}{x-x'} = p_f(x,t) - \sigma_o - \sigma_{coh}(w(x,t)), \quad x, x' \in [-\ell, \ell] \tag{3}$$

where $E' = E/(1-\nu^2)$ is the plane-strain modulus, ν the Poisson's ratio of the material. In view of the problem symmetry, the previous integral equation can be conveniently written for on one-wing of the fracture:

$$\frac{E'}{4\pi}\int_{0}^{\ell}\left(\frac{1}{x-x'} - \frac{1}{x'+x}\right)\frac{\partial w(x',t)}{\partial x'}\mathrm{d}x' = p_f(x,t) - \sigma_o - \sigma_{coh}(w(x,t)), \quad x, x' \in [0, \ell] \tag{4}$$

Due to the presence of cohesive forces and the traction separation law, this boundary integral equation is non-linear.

Using a cohesive zone model, the fracture advance $\ell(t)$ is based on the stress component σ_{yy} perpendicular to the fracture plane ahead of the current fracture tip. In other words, the fracture propagates when

$$\sigma_{yy}(x = \ell) = \sigma_c \tag{5}$$

It is worth pointing out that at any given time, the cohesive forces cancel the stress singularity at the fracture tip that would be otherwise present. The stress intensity factor K_I must thus be zero at all times. For a pure mode I crack, the stress intensity factor is obtained via the weight function approach directly from the profile of the net loading (Bueckner, 1970; Rice, 1972):

$$K_I = \frac{2\sqrt{\ell}}{\sqrt{\pi}}\int_0^{\ell}\frac{p_f(x,t) - \sigma_o - \sigma_{coh}(w(x,t))}{(\ell^2 - x^2)^{1/2}}\,\mathrm{d}x = 0 \tag{6}$$

The requirement $K_I = 0$ can be altenatively used as a propagation condition, or checked a posteriori as an error estimate.

2.2. Laminar lubrication flow in a rough tensile fracture

Under the lubrication approximation, for an incompressible fluid and an impermeable medium (negligible leak-off), the fluid mass conservation in the deformable fracture reduces to

$$\frac{\partial w}{\partial t} + \frac{\partial q}{\partial x} = 0 \text{ in the fluid filled part } x \in [0,\ell_f] \tag{7}$$

where $q(x,t)$ is the local fluid flux inside the fracture and $\ell_f(t)$ denotes the current fluid front position.

As the aperture is small near the tip and especially in the cohesive zone, it can not be considered as much larger than its small scale spatial variation - i.e. its roughness. The rough surfaces in possibly partial contact in the cohesive zone results in a decrease of the hydraulic transmissivity of the fracture compared to the cubic law. This has been observed in a large number of flow experiments under laminar condition in rock joints under different normal stress (Fig. 1). A number of empirical approximations have been put forward in literature to describe such a deviation from the cubic Poiseuille's law observed in the laminar regime. A typical approach consists in introducing a friction/correction factor f in Poiseuille's law relating fluid flux to the pressure gradient:

$$q = -\frac{w^3}{\mu' f}\frac{\partial p_f}{\partial x}, \qquad 0 < x < \ell_f, \quad f = 1 + \alpha_c \times \left(\frac{w_R}{w}\right)^{\alpha_e} \tag{8}$$

where $\mu' = 12\mu$ is the effective fluid viscosity. w_R quantifies the fracture roughness, and is for example, taken as the peak asperity height or the standard deviation of the aperture (see Table. 1). It grasps the width scale characterizing the deviation from the cubic law. α_c and α_e are experimentally determined parameters dependent on the fractal properties of the self-affine rough fracture surfaces (Talon et al., 2010; Jin et al., 2017). Interestingly, the fracture roughness properties are also related to the size of the process zone, above and below which the off-plane height variation may present different roughness exponents (Mourot et al., 2005; Bonamy et al., 2006; Ponson et al., 2007; Morel et al., 2008). Moreover, a process zone length scale can be extracted from the spatial correlations of the slopes of a rough fracture surface (Vernède et al., 2015). Fracture roughness therefore appears to correlate with both the process zone w_c and the fluid flow deviation w_R width scales, yet the exact relation between

w_c and w_R has not been clearly deciphered to our knowledge. On the account that w_R and $w_c \sim 1-500\mu$m in most rocks (Renshaw, 1995; Garagash, 2015, 2019), we assume $w_R \approx w_c$. One has to note, that α_c and α_e are fitted from experiments and α_c is not independent of the choice of w_R - $\alpha_c \times w_R^{\alpha_e}$ is the controlling constant when expanding Eq. (8). α_e governs the power-law dependence of the friction factor with the mechanical width w. The number of experiments dedicated to flow in rough fractures provide a guideline for α_c and α_e although a significant scatter can be observed (see Table. 1). In the following, we assume $\alpha_c = 1$ (and $w_R = w_c$) for simplicity in order to investigate the mechanism associated with fracture roughness although we recognize that it may not be the case. The friction factor therefore reduces to

$$f = 1 + \left(\frac{w_c}{w}\right)^{\alpha_e} \tag{9}$$

where $\alpha_e = 0$ in the smooth fracture limit. For the case of a rough fracture, we will perform simulations for $\alpha_e = 2$ which corresponds to the largest power-law exponent reported experimentally (and as such will lead to the largest impact of fracture roughness). The resulting deviation between mechanical and hydraulic aperture for such a simplified fluid flow deviation model (9) is illustrated in Fig. 2.

2.3. Boundary and initial conditions

The fluid is injected at the fracture center at a constant injection rate Q_o (in m^2/s under plane-strain conditions), such that the flow entering one-wing of the fracture is:

$$q(x = 0^+, t) = Q_o/2 \tag{10}$$

which can be alternatively be accounted by the global fluid volume balance, integrating the continuity equation (7) for the fluid:

$$2\int_0^{\ell_f(t)} w(x,t)\mathrm{d}x = Q_o t \tag{11}$$

In the fluid lag near the fracture tip, the fluid is vaporized and its pressure is equal to the cavitation pressure p_{cav}, which is typically much smaller than the liquid pressure p_f in the

w_R definition	Reference	α_e	α_c	w_R (μm)
Standard deviation of the aperture	Renshaw (1995) *	2	1.5	Basalt (1.6), marble (13) granite (0.63-320), granodiorite (500)
	Zimmerman & Bodvarsson (1996) *	2	1.5	Granite (34-295)
	Garagash (2015)	1	1	Concrete (150)
Peak asperity height	Lomize (1951)	1.5	6.0	Sand-coated glass
	Zhang et al. (2015)	1.12	10^{-3}	Granite (2320-3140), limestone (4050)

Table 1: Different empirical models suggested in literature for the friction factor (Eq. (8)). The superscript * indicates that the expression of the friction factor reported does not exactly correspond to the functional form of Eq. (8). As a result, for those cases, we obtain α_c, α_e from the two leading terms of a Taylor expansion of the reported expression.

fluid filled part and the in-situ confining stress σ_o. We thus have the following pressure boundary condition in the lag:

$$p_f(x,t) = p_{cav} \approx 0, \quad x \in [\ell_f(t), \ell(t)] \tag{12}$$

The fluid front velocity $\dot{\ell}_f$ is equal to the mean fluid velocity q/w at that fluid front location $x = \ell_f$ (Stefan condition):

$$\dot{\ell}_f = - \left. \frac{w^2}{\mu' f(w)} \frac{\partial p_f}{\partial x} \right|_{x=\ell_f} \tag{13}$$

The fracture opening is zero at the fracture tip taken as the beginning of the cohesive zone:

$$w(x = \ell, t) = 0 \tag{14}$$

Initial conditions. We model the nucleation process, and the coupled developments of the cohesive zone and the fluid lag. We start from a negligibly small fracture in which cohesive forces have not completely vanishes: the fracture length equals the cohesive zone length initially. Upon the start of injection, this initially static flaw is fully filled with fluid at a pressure slightly larger than the in-situ stress σ_o.

2.4. Energy balance

The energy balance for a propagating hydraulic fracture can be constructed by combining two separate energy balance equations, one for the viscous fluid flow and the other one for the quasi-brittle medium deformation of an advancing crack (Lecampion & Detournay, 2007). The external power $P_e = Q_o p_{f0}$ (where $p_{f0} = p_f(x = 0, t)$ is the fluid pressure at the inlet) provided by the injecting fluid is balanced by five terms:

- the rate of work done to overcome the in-situ confining stress: $\dot{W}_o = Q_o \sigma_o$
- the rate of change of the elastic energy stored in the solid $\dot{W}_e$:

$$\dot{W}_e = \int_0^{\ell_f} p \frac{\partial w}{\partial t} \mathrm{d}x + \int_0^{\ell_f} w \frac{\partial p}{\partial t} \mathrm{d}x - \sigma_o \int_{\ell_f}^{\ell} \frac{\partial w}{\partial t} \mathrm{d}x \tag{15}$$

- a power associated with the rate of the change of the fluid lag cavity volume times the in-situ far-field stress $\dot{W}_l$:

$$\dot{W}_l = 2\sigma_o \frac{\mathrm{d}}{\mathrm{d}t} \int_{\ell_f}^{\ell} w \mathrm{d}x \tag{16}$$

- the viscous dissipation rate in the fluid filled region of the fracture D_v:

$$D_v = -2 \int_0^{\ell_f} q \frac{\partial p}{\partial x} \mathrm{d}x \tag{17}$$

- the energy rate associated with the debonding of cohesive forces and the creation of new fracture surfaces D_k:

$$D_k = -\int_0^{\ell} w \frac{\partial \sigma_{coh}}{\partial t} \mathrm{d}x + \int_0^{\ell} \sigma_{coh} \frac{\partial w}{\partial t} \mathrm{d}x. \tag{18}$$

Accounting for the symmetry of the problem, we can define an apparent fracture energy

$$G_{c,app} = \frac{D_k}{2\dot{\ell}} \tag{19}$$

In the coordinate system of the moving tip, we can rewrite Eq. (19) for the linear weakening cohesive zone model as follows (see more details in Supplemental Materials):

$$G_{c,app} = \frac{1}{2}\sigma_c w(\hat{x} = \ell_{coh}) + \frac{1}{2\dot{\ell}}\sigma_c \int_0^{\ell_{coh}} \left.\frac{\partial w}{\partial t}\right|_{\hat{x}} \mathrm{d}\hat{x}, \quad \hat{x} = \ell - x \tag{20}$$

When the fracture has already nucleated and the cohesive zone size is negligible compared to the fracture length ($\ell \gg \ell_{coh}$), the first term in Eq. (20) equals the real fracture energy G_c with $w(\hat{x} = \ell_{coh}) = w_c$. For a large fracture, where the cohesive zone is nearly constant, the second term tends to zero as the material time derivative of width is negligible for fracture with slow variation of velocity: more precisely, in the tip reference frame the convective derivative $\dot{\ell}\frac{\partial \cdot}{\partial \hat{x}}$ (which leads when integrated to the first term) dominates over the material time derivative $\frac{\partial \cdot}{\partial t}|_{\hat{x}}$. As a result, the apparent energy tends to equal to the real fracture energy $G_{c,app} \approx G_c$ at large time. However, it does not necessarily imply that the fracture width asymptote in the near tip region follows the LEFM limit. It only results from the fact that the convective derivative dominates - and as such the travelling semi-infinite fracture solution of Garagash (2019) applies (where different tip asymptotes emerge as function of the ratio σ_o/σ_c). However the equivalence $G_{c,app} = G_c$ does not hold when the fracture length is comparable to the cohesive zone $\ell \geq \ell_{coh}$. The first term increases with time until $w(\hat{x} = \ell_{coh})$ reaches the critical opening w_c at nucleation while the second term results from the competition between the fracture velocity and the material rate change of the volume embedded inside the cohesive zone. As a result of this second term, the evolution of the apparent fracture energy may not be necessarily monotonic in an intermediate phase as we shall see later from our numerical simulations.

3. Structure of the solution

Before investigating the problem numerically, we discuss the evolution of such a quasi-brittle HF in light of dimensional analysis. We notably highlight the difference brought upon the existence of a process zone compared to the linear elastic fracture mechanics case (Garagash & Detournay, 2005; Garagash, 2006; Lecampion & Detournay, 2007). Following previous work on hydraulic fracturing (Garagash, 2000; Detournay, 2004), we scale the flux q with the injection rate Q_o, and scale the fracture width w, net pressure $p_f - \sigma_o$, fracture length ℓ, and the extent of the liquid filled part of the fracture ℓ_f introducing corresponding width W, pressure P, fracture length L and fluid extent L_f characteristic scales:

$$w(x,t) = W(t)\Omega(\xi,\mathcal{P}), \quad p_f(x,t) - \sigma_o = P(t)\Pi(\xi,\mathcal{P}), \quad q(x,t) = Q_o\Psi(\xi,\mathcal{P}) \tag{21}$$

$$\ell(t) = L(t)\gamma(\mathcal{P}), \quad \ell_f(t) = L_f(t)\gamma_f(\mathcal{P}) \tag{22}$$

where $\xi = x/\ell$ is a dimensionless coordinate. The dimensionless variables also depend on one or more dimensionless number $\mathcal{P}$ (which may depend on time). Introducing such a scaling in the governing equations of the problem allows to isolate different dimensionless groups associated with the different physical mechanisms at play (elasticity, injected volume, viscosity, fracture energy) and define relevant scalings.

Before going further, we briefly list the dimensionless form of the governing equations and the expression of the different dimensionless groups appearing in the governing equations (1)-(14).

- The elasticity equation can be re-written as:

$$\Pi - \Sigma_{coh}(\Omega(\xi)) = \mathcal{G}_e \frac{1}{4\pi}\frac{1}{\gamma}\int_0^1 \frac{\partial\Omega}{\partial\xi}\left(\frac{1}{\xi-\xi'} - \frac{1}{\xi+\xi'}\right)\mathrm{d}\xi', \quad 0 < \xi, \xi' < 1 \tag{23}$$

  with $\mathcal{G}_e = \dfrac{WE'}{PL}$ and the dimensionless traction-separation law as

$$\Sigma_{coh} = \mathcal{G}_t \times \left(1 - \frac{\Omega}{\mathcal{G}_w}\right), \quad \Omega < \mathcal{G}_w \tag{24}$$

  with $\mathcal{G}_t = \sigma_c/P$ and $\mathcal{G}_w = w_c/W$.

- The dimensionless fluid continuity and roughness corrected Poiseuille's law are better expressed by scaling the spatial coordinate with the fluid front position - thus introducing the ratio of scales $\mathcal{G}_l = L_f/L$ - $\hat{\xi} = x/\ell_f = \xi \times (\gamma/\gamma_f)/\mathcal{G}_l$:

$$t\frac{\partial\Omega}{\partial t} + t\frac{\dot{W}}{W}\Omega + \mathcal{G}_v\frac{1}{\gamma_f}\frac{\partial\Psi}{\partial\hat{\xi}} = 0 \tag{25}$$

$$\Psi = -\frac{1}{\mathcal{G}_m}\frac{\Omega^3}{f \times \gamma_f}\frac{\partial\Pi}{\partial\hat{\xi}} \tag{26}$$

  with $\mathcal{G}_v = \dfrac{Q_o t}{WL_f}$ related to the fracture volume, and $\mathcal{G}_m = \dfrac{\mu' Q_o L_f}{PW^3}$ related to fluid viscosity, while the friction roughness correction f can be simply re-written as $f = 1 + (\mathcal{G}_w/\Omega)^{\alpha_e}$.

- the entering flux boundary conditions becomes

$$\Psi(\xi = 0^+,t) = 1/2 \tag{27}$$

while the dimensionless net pressure Π in the fluid lag is

$$\Pi(\xi \leq \xi_f = \ell_f/\ell) = -\mathcal{G}_o = -\frac{\sigma_o}{P} \tag{28}$$

It is worth noting that for the linear weakening law the dimensionless fracture energy is simply $\mathcal{G}_c = (w_c\sigma_c)/(2PW) = \frac{1}{2}\mathcal{G}_w\mathcal{G}_t$. In addition, in order to make the link with the LEFM scalings that use a reduced fracture toughness defined as $K' = \sqrt{32/\pi}K_{Ic}$, we use the equivalent dimensionless fracture toughness: $\mathcal{G}_k = \sqrt{32/\pi}\sqrt{\mathcal{G}_e\mathcal{G}_c} = \sqrt{16/\pi}\sqrt{\mathcal{G}_e\mathcal{G}_w\mathcal{G}_t}$ in the following.

The well-known scalings under the LHFM assumptions for the case of negligible lag ($\mathcal{G}_l = L_f/L = 1$) are obtained by recognizing that elasticity is always important ($\mathcal{G}_e = 1$), and the fact that without fluid leak-off the fracture volume equals the injected volume at all time ($\mathcal{G}_v = 1$). The viscosity and toughness scalings are then obtained by either setting $\mathcal{G}_m$ (M/viscous scaling) or $\mathcal{G}_k$ (K/toughness scaling) to unity. Alternatively, the fluid lag dominated scaling (O-vertex) is obtained by recognizing that viscous effects are necessary for cavitation to occur ($\mathcal{G}_m = 1$) and the lag covers a significant part of the fracture such that the pressure scale is given by the in-situ stress ($\mathcal{G}_o = 1$). Similarly elasticity ($\mathcal{G}_e = 1$) and fluid volume ($\mathcal{G}_v = 1$) are driving mechanisms. These well-known scalings for the different limiting propagation regimes are recalled in Table 2.

Under the assumption of linear elastic fracture mechanics, as discussed in Garagash (2006); Lecampion & Detournay (2007), a plane-strain HF evolves from an early-time solution where the fluid lag is maximum to a late solution where the fluid and fracture front coalesces (zero lag case) over a time-scale

$$t_{om} = \frac{E'^2\mu'}{\sigma_o^3} \tag{29}$$

This time-scale directly emerges as the time it takes for the dimensionless in-situ stress $\mathcal{G}_o$ to reach unity in the zero lag scalings. In addition, the solution also depends on a dimensionless toughness $\mathcal{K}_m$ (or alternatively dimensionless viscosity) independent of time. The fluid lag is the largest for small dimensionless toughness and is negligible at all time for large dimensionless toughness. The propagation can thus be illustrated via a triangular phase diagram, whose three vertices (O-M-K) corresponds to three limiting regimes. The O-vertex corresponds to the limiting case of a large lag / negligible toughness, the M-vertex corresponds to viscosity dominated propagation with a negligible fluid lag while the K-vertex corresponds to a toughness dominated propagation where viscous effects are always negligible and as a result no fluid lag exists.

The introduction of a cohesive zone modifies partly this propagation diagram. One can define a cohesive zone scaling (which will be coined with the letter C) by setting the pressure scales P to the peak cohesive stress σ_c ($\mathcal{G}_t = 1$), the opening scale W to the critical opening w_c ($\mathcal{G}_w = 1$). We then readily obtain from elasticity ($\mathcal{G}_e = 1$) that the fracture characteristic length L equals the classical cohesive characteristic length scale (Rice, 1968; Hillerborg et al., 1976):

$$L_{coh} = \frac{E' w_c}{\sigma_c} \tag{30}$$

Such a scaling is relevant at early time when the cohesive zone scale is of the order of the fracture length. We know from the LHFM limit that the fluid lag is also important at early time. From lubrication flow, combining fluid continuity and Poiseuille's law to obtain the Reynolds equation enables to define the corresponding fluid front scale L_f as $w_c\sqrt{\sigma_c t/\mu'}$ (by setting the resulting dimensionless group $\mathcal{G}_v/\mathcal{G}_m$ in the Reynolds equation to one). Another time-scale t_{cm} thus emerges as the characteristic time for which the fluid front in that cohesive scaling is of the same order of magnitude than the characteristic fracture / cohesive length:

$$t_{cm} = \frac{E'^2 \mu'}{\sigma_c^3} = t_{om} \times \left(\frac{\sigma_o}{\sigma_c}\right)^3. \tag{31}$$

This time-scale quantifies the time required for the cohesive zone to develop in relation to the penetration of the fluid. It is worth noting that the ratio of time-scales t_{cm}/t_{om} related to the fluid lag in the cohesive (C) and LHFM (O) scalings is directly related to the ratio between the in-situ confining stress and the peak cohesive stress.

Three stages of growth can thus be delineated as function of the evolution of the cohesive zone.

- Stage I for early time ($t \ll t_{cm}$): the whole fracture length is embedded inside the cohesive zone. The cohesive zone develops with time yet is not fully nucleated. We will refer to this stage as the nucleation stage in the following.

- Stage II for intermediate times (of the order of t_{cm}): the cohesive zone has now fully nucleated and part of the fracture surfaces are completely separated without cohesion ($w > w_c$ in the central part of the fracture). The cohesive zone remains important compared to the whole fracture length and may be not yet stabilized. We will refer to this stage as the intermediate propagation stage.

- Stage III ($t \gg t_{cm}$): the cohesive zone now only takes up a very small fraction of the whole fracture such that the small-scale-yielding assumption becomes valid. We will refer to this stage as the late time propagation stage/small-scale-yielding stage.

From the different scalings in Table 2, we see that using t_{cm} as a characteristic time-scale, the evolution of a HF in a quasi-brittle material depends only on i) a dimensionless toughness $\mathcal{K}_m$, ii) the ratio between the confining stress and material strength σ_o/σ_c and iii) the dimensionless roughness exponent α_e. Possibly, a value different than unity for the coefficient α_c in relation to the flow-roughness relationship (8) would also play a role.

For a quasi-brittle impermeable material, the propagation can be schematically grasped by the propagation diagram depicted on Fig. 3. The propagation starts in a cohesive / nucleation regime (vertex C) and ultimately ends up at large time on the M-K edge (LHFM / small-scale-yielding limit) at a point depending on the (time-independent) dimensionless toughness $\mathcal{K}_m$. How the fracture evolves from the nucleation (vertex C) stages to the large time LHFM limits is function of the ratio σ_o/σ_c as well as the roughness exponent. When $\sigma_o \ll \sigma_c$ ($t_{cm} \ll t_{om}$), the cohesive zone develops faster than the time required for the fluid front to coalesce with the fracture front. In that case, the small-scale-yielding assumption may become valid early in conjunction with the presence of a fluid lag (O-K edge) - the fluid

	C	O	M	K
L	$L_{coh} = \dfrac{E' w_c}{\sigma_c}$	$\dfrac{E' Q_o^{1/2} \mu'^{1/4} t^{1/4}}{\sigma_o^{5/4}}$	$\dfrac{E'^{1/6} Q_o^{1/2} t^{2/3}}{\mu'^{1/6}}$	$\dfrac{E'^{2/3} Q_o^{2/3} t^{2/3}}{K'^{2/3}}$
P	σ_c	σ_o	$\dfrac{E'^{2/3} \mu'^{1/3}}{t^{1/3}}$	$\dfrac{K'^{4/3}}{E'^{1/3} Q_o^{1/3} t^{1/3}}$
W	w_c	$\dfrac{Q_o^{1/2} \mu'^{1/4} t^{1/4}}{\sigma_o^{1/4}}$	$\dfrac{Q_o^{1/2} \mu'^{1/6} t^{1/3}}{E'^{1/6}}$	$\dfrac{K'^{2/3} Q_o^{1/3} t^{1/3}}{E'^{2/3}}$
L_f/L	$(t/t_{cm})^{1/2}$	$(t/t_{om})^{1/2}$	1	1
$\mathcal{G}_m$	$(16/\pi)^2 \mathcal{K}_m^{-4} (t/t_{cm})^{1/2}$	1	1	$\mathcal{K}_m^{-4}$
$\mathcal{G}_k$	$(16/\pi)^{1/2}$	$\mathcal{K}_m = \dfrac{K'}{E'^{3/4} Q_o^{1/4} \mu'^{1/4}}$	$\mathcal{K}_m$	1
$\mathcal{G}_o$	σ_o/σ_c	1	$(t/t_{om})^{1/3}$	$(t/t_{om})^{1/3} \mathcal{K}_m^{-4/3}$
$\mathcal{G}_w$	1	$\left(\dfrac{t_{cm}}{t}\dfrac{\sigma_o}{\sigma_c}\right)^{1/4} \dfrac{\pi}{16}\mathcal{K}_m^2$	$\left(\dfrac{t_{cm}}{t}\right)^{1/3} \dfrac{\pi}{16}\mathcal{K}_m^2$	$\left(\dfrac{t_{cm}}{t}\right)^{1/3} \dfrac{\pi}{16}\mathcal{K}_m^{4/3}$

Table 2: Characteristic scales and dimensionless numbers governing the evolution of a plane-strain quasi-brittle HF in the different limiting regimes: C - lag/cohesive/nucleation, O - lag/viscous/ LHFM, M - fully filled/viscous/LHFM, K - fully filled/toughness/LHFM. The evolution of the HF is also function of the dimensionless roughness exponent α_e. The time-scales t_{om} and t_{cm} defined in Eqs (29), (31) are related as $t_{cm}/t_{om} = (\sigma_o/\sigma_c)^3$. The $16/\pi$ factors appearing in the dimensionless numbers are due to the use of $K' = \sqrt{32/\pi} K_{Ic}$ in the LHFM based scalings (Detournay, 2004; Garagash, 2006) and the fact that for the linear weakening cohesive law $G_c = w_c \sigma_c / 2$.

front will lie outside of the cohesive zone for some time. On the other limit, for $\sigma_o > \sigma_c$, the fluid front tends to remain inside the cohesive zone which develops slower than the fluid front progress.

How exactly, the growth of the HF is influenced by the interplay between the cohesive zone and lag evolution for different values of σ_o/σ_c, dimensionless toughness and fracture roughness intensity will be now investigated numerically.

4. Numerical scheme

In order to decipher the interplay between the fluid front and cohesive zone, it is necessary to account for the nucleation of both the cohesive zone and the fluid lag. Previous numerical

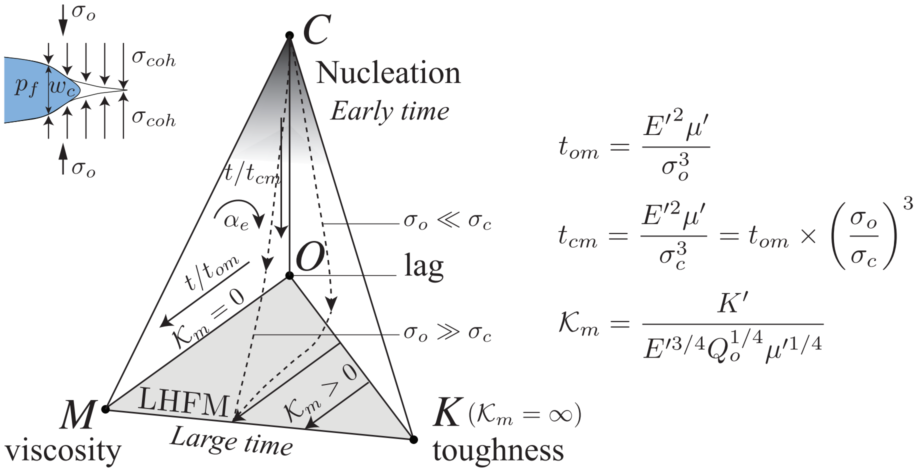

Figure 3: Propagation diagram of a plane-strain hydraulic fracture with a rough cohesive fracture tip. The bottom $O-M-K$ triangle corresponds to the LHFM limit. Note that possibly, a value of α_c (see Eq. (8)) different than unity will impact the solution.

investigation using LHFM either tracks explicitly the fluid front in addition to the fracture front (Lecampion & Detournay, 2007; Zhang et al., 2005; Gordeliy & Detournay, 2011) or uses a cavitation algorithm introducing a fluid state variable $\theta \in [0,1]$ (1 for the liquid phase, 0 for the vapour phase) (Shen, 2014; Mollaali & Shen, 2018) in a similar way than thin-film lubrication cavitation models (see for example Szeri (2010)).

The cavitation approach enables the spontaneous nucleation of the fluid lag but adds another variables and additional inequalities conditions ($p_f \geq 0, 0 \leq \theta \leq 1, p_f(1-\theta) = 0$) in each element. The computational cost of such cavitation schemes increases significantly as quadratic programing problem needs to be solved at each time-step. We therefore propose here an algorithm taking advantage of both the cavitation scheme at early time (when the fluid lag nucleates from an initially fully liquid filled flaw) and a fluid-front-tracking scheme at later times.

Our algorithm consists of the use of two successive schemes, both based on a fixed regular grid with constant mesh size. At the beginning of the simulation, we adopt an Elrod-Adams type scheme similar to the one described in Mollaali & Shen (2018). This scheme automatically captures the appearance of the fluid lag in the most accurate manner (Liu & Lecampion, 2019b). In a second stage of the simulation, we use the results of the previous algorithm to initialize a scheme similar to Gordeliy & Detournay (2011) where the fluid front position is tracked explicitly via the introduction of a filling fraction variable in the partly filled element at the lag boundary. We discretize respectively the elasticity and fluid mass conservation using a displacement discontinuity method with piece-wise constant elements and finite difference. We use an implicit time-integration scheme to solve iteratively for the fluid pressure and the associated opening. An additional outer loop solves for the time-step increment corresponding to a fixed increment of fracture length. More details are given in Appendix A.

Mesh requirements. A sufficient number of cohesive elements is necessary to ensure the stress accuracy ahead of the fracture tip and the resolution of the fracture propagation condition. A minimum of three elements are suggested to mesh the cohesive zone to ensure sufficient accuracy of the near tip stress field (Falk et al., 2001; Moës & Belytschko, 2002; Turon et al., 2007). In dry fracture mechanics, the technique of artificially enlarging the cohesive zone length while keeping the fracture energy constant is often used (increasing w_c and decreasing σ_c accordingly) (Bazant & Planas, 1997; Turon et al., 2007) thus allowing the use of coarser meshes. Unfortunately, such a technique is not adequate for cohesive hydraulic fractures. It is only valid when the confining σ_o is adjusted together with σ_c in order to keep the ratio of time scales t_{cm}/t_{om} unchanged (see Eq. (31)). If not, this will change the physics of the fluid front-cohesive zone coupling. Another important difference with dry fracture mechanics is the fact that the fracture propagates in a medium under initially compressive state of stresses, as such the tensile region ahead of the fracture shrinks as the confinement increases. Assuming a fluid lag the same size as the cohesive zone, Fig. 4 displays the evolution of the tensile zone ahead of the fracture tip as the uniformly pressurized HF grows under different confinements. The tensile zone significantly shrinks as the confining stress increases, and therefore requires for a finer mesh. Such a confinement-related mesh requirement has been seldomly discussed in previous studies (Chen et al., 2009; Chen, 2012;

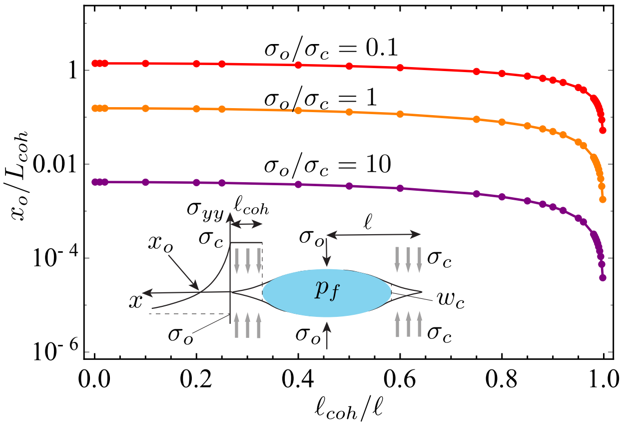

Figure 4: Evolution of the size of the tensile zone ahead of the fracture tip with the cohesive fraction for different confining to peak cohesive stress ratios. The pressure is uniform everywhere inside the fracture but no fluid is allowed to enter the cohesive zone (Dugdale cohesive zone model).

Sarris & Papanastasiou, 2011; Carrier & Granet, 2012; Salimzadeh & Khalili, 2015; Wang, 2015; Li et al., 2017) where the fluid front-cohesive zone coupling is often neglected (zero fluid lag, small cohesive zone) and the simulation performed under zero confinement. In this paper, we release the confinement-related requirement by adapting the time-step for a given fixed fracture increment to fulfill the propagation stress propagation condition. We also check a posteriori that the stress intensity factor is indeed null using Eq. (6). We obtain an absolute error on Eq. (6) of about 5% (in a range between 0.1 and 8%) for all the reported simulations.

Apart from the tensile zone ahead of the fracture tip, one also needs to resolve the fluid lag which shrinks tremendously as the fracture grows but still influences the solution (Garagash, 2019). At least one partially-filled (lag) element is necessary to account for the influence of the fluid cavity on the tip stress field. At large time, the fluid lag becomes negligible compared to the cohesive zone. This is ultimately the bottle-neck governing the computational burden due to the mesh requirement of at minima one element in the fluid lag. For all the results presented in the following, we actually stop the simulations when the fluid fraction $\xi_f = \ell_f/\ell$ reached 0.99 or when the fracture length was already within five percent of the LHFM solutions.

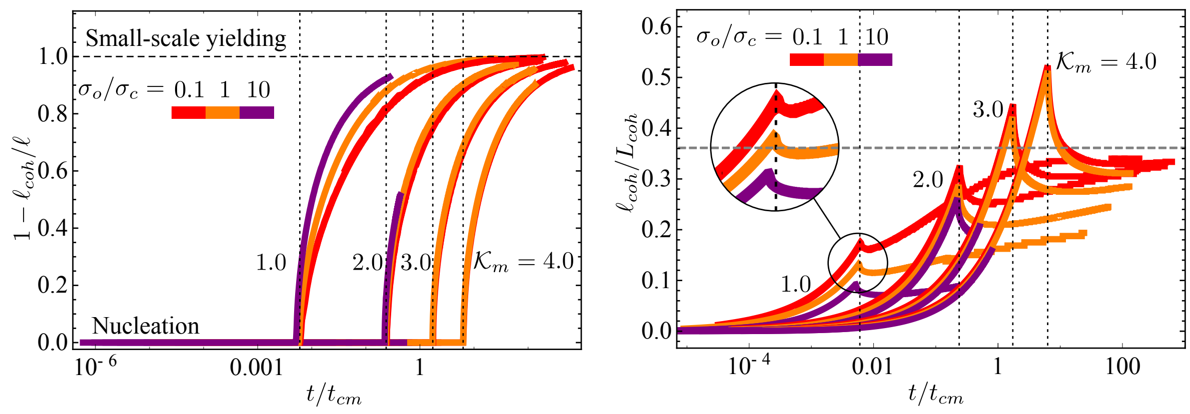

a) b)

Figure 5: Evolution of a) the non-cohesive fraction $1-\ell_{coh}/\ell$ and b) dimensionless cohesive length ℓ_{coh}/L_{coh} with t/t_{cm} for $\mathcal{K}_m = 1-4$. The red, orange, and purple curves correspond to $\sigma_o/\sigma_c = 0.1, 1.0, 10$ respectively. The dotted vertical lines indicate the cohesive zone nucleation period for $\sigma_o/\sigma_c = 0.1$, $\mathcal{K}_m = 1 - 4$. The dashed horizontal line represents the small-scale yielding asymptote ($\approx 0.115\pi$) of the cohesive zone length for the linear-softening cohesive model (Dempsey et al., 2010).

5. Results

We now numerically explore the propagation diagram described in Fig. 3. We perform a series of simulations covering dimensionless toughness from 1 to 4 and different level of confining to peak cohesive stress ratio σ_o/σ_c from 0.1 to 10 for either a smooth ($\alpha_e = 0$) or rough ($\alpha_e = 2$) fracture. These conditions span the transition from viscosity to toughness dominated growth regimes, as well as laboratory ($\sigma_o/\sigma_c = 0.1 - 1$) and field conditions ($\sigma_o/\sigma_c = 10$).

5.1. A smooth cohesive fracture ($\alpha_e = 0$)

The three stages related to nucleation, intermediate and late time propagation are well visible on the time evolution of the dimensionless cohesive length (Fig. 5), apparent fracture energy (Fig. 6), fracture length (Fig. 9), as well as inlet width (Fig. 10) and net-pressure (Fig. 11).

Cohesive zone growth. The scaled cohesive length ℓ_{coh}/L_{coh} evolves non-monotonically with time (Fig. 5). This evolution is dependent on both the dimensionless toughness $\mathcal{K}_m$ and

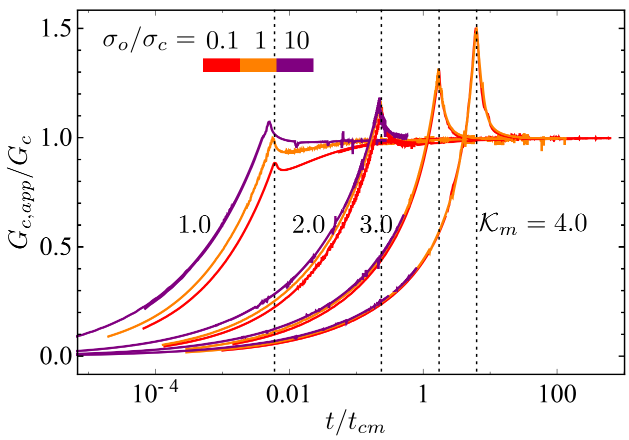

Figure 6: Smooth cohesive fracture tip: evolution of the apparent fracture energy $G_{c,app}/G_c$ with t/t_{cm} for $\mathcal{K}_m = 1-4$. The red, orange, and purple curves correspond to $\sigma_o/\sigma_c = 0.1, 1.0, 10$ respectively. The dotted vertical lines indicate the cohesive zone nucleation period for $\sigma_o/\sigma_c = 0.1$, $\mathcal{K}_m = 1-4$.

σ_o/σ_c. At early time during the nucleation phase, when the fracture length is completely embedded inside the cohesive zone ($1-\ell_{coh}/\ell = 0$), the cohesive zone increases monotonically (Fig. 5). We define the time t_c as the end of the nucleation phase, when here after $1-\ell_{coh}/\ell > 0$. From our simulations, we found that t_c follows approximately an exponential relation $t_c/t_{cm} \sim \mathcal{K}_m^{5.17}$ for $\mathcal{K}_m \in [1-4]$. This exponent is consistent with the range of exponents in the viscosity ($t_c/t_{cm} \sim \mathcal{K}_m^6$) and toughness ($t_c/t_{cm} \sim \mathcal{K}_m^4$) dominated regimes which can be obtained by setting $\mathcal{G}_w = W/w_c = 1$ in respectively the M- and K-scaling in Table 2. In addition, t_c also slightly depends on the dimensionless confinement σ_o/σ_c, see the inset on Fig. 5. Larger confinement slightly reduces this nucleation period for a given $\mathcal{K}_m$. The cohesive zone length at nucleation are larger for larger dimensionless toughness and then decreases with time after nucleation.

At large time, we observe that - at least for low dimensionless confinement - the cohesive zone length tends to a similar value for all dimensionless toughness. Unfortunately, this is less observable for larger dimensionless confinement which leads to prohibitive computational cost such that the simulations were stopped prior to stabilization of the cohesive zone length. However, the trend for $\sigma_o/\sigma_c = 1$ hints that a similar behavior holds for larger confinement albeit possibly much later in time.

Associated energy dissipation. The energy spent in debonding cohesive forces (apparent fracture energy) increases similarly to the growth of the cohesive zone length (Fig. 6). This is due to the fact that $\dot{\ell} \approx \dot{\ell}_{coh}$ during the nucleation stage. Interestingly, the apparent fracture energy may even go above the fracture energy G_c at nucleation for large dimensionless toughness / large dimensionless confinement as illustrated in Fig. 6. At large time, the apparent fracture energy converges to the fracture energy G_c, confirming the fact that the material derivative of width (in the moving tip frame) becomes negligible in Eq. (20). This confirms that at large time (when $1 - \ell_{coh}/\ell \sim 1$) one can use the solution of a steadily moving semi-infinite hydraulic fracture solution accounting for cohesive forces (Garagash, 2019). However, care must be taken to use such a semi-infinite fracture solution when the cohesive zone length is of the same order than the overall fracture length. For example, the results obtained in Garagash (2019) based on the use of an equation of motion and the semi-infinite cohesive HF solution lead to cohesive zone length larger than the finite fracture length under the premises of the constant apparent fracture energy. This ultimately leads to an over-estimation of fracturing energy dissipation and larger deviation from LEFM solutions as it neglects the evolution of the apparent fracture energy associated with the nucleation phase.

Comparisons with linear hydraulic fracture mechanics (LHFM). The time evolution of dimensionless fracture length (scaled by the viscosity dominated LHFM growth length scale $L_m(t)$ - see Table. 2) is displayed as dashed curves on Fig. 9. The corresponding inlet net-pressure and width evolution for the smooth cohesive zone are displayed as dashed curves on Fig. 10 and 11 respectively. Our results indicate that the CZM solutions converge toward the LHFM ones (for the corresponding dimensionless toughness) at large times $t \gg t_{cm}$. The exact dimensionless time for such a convergence toward the LHFM solution is larger for larger dimensionless toughness, and smaller for larger σ_o/σ_c.

Interestingly, the fracture length is larger at the early stage of growth compared to the LHFM estimate while the inlet opening and pressure are smaller. These differences directly result from the fact that the cohesive forces greatly increases the fluid lag size and impacts its evolution during the nucleation and intermediate stages of growth. Indeed, in the LHFM case, the fluid lag is negligible at all times for dimensionless toughness $\mathcal{K}_m$ larger than ~ 1.5 as reported in Garagash (2006); Lecampion & Detournay (2007). For $\mathcal{K}_m = 1$, the fluid fraction in the LHFM case is already small at early time: it evolves from 0.9 (when $t \ll t_{om}$) to 1 (for $t \approx t_{om}$, see Fig. A.18 in appendix). For the same dimensionless toughness, the fluid fraction is lower than 0.6 at early time when accounting for the cohesive zone (see Fig. 12). The large extent of the fluid lag is similarly found for larger dimensionless toughness - a striking difference with the LHFM case for which no fluid lag is observed for $\mathcal{K}_m > 1.5$. The cohesive forces significantly enhance the suction effect and thus lag size during nucleation. For the same value of $\mathcal{K}_m$, a larger confinement compared to peak strength (larger σ_o/σ_c) decreases the lag size. Larger σ_o/σ_c results in steeper fluid pressure gradient and accelerates the penetration of the fluid front into the cohesive zone during the nucleation and intermediate phase (see Fig. 13) .

As the dimensionless toughness increases, the effect of σ_o/σ_c becomes limited to the nucleation phase (see the length, inlet width and inlet net pressure evolution on Figs. 9, 10, 11). After nucleation, the solutions appear independent of σ_o/σ_c for $t > t_{cm}$ for the $\mathcal{K}_m = 3$ and 4 cases. The fact that σ_o/σ_c does not influence the growth after nucleation for large toughness can be traced back to the fact that the fluid lag cavity is very small in comparison to the cohesive zone length as can be seen on Fig. 13.

Fig. 7 displays the dimensionless fracture length, fluid fraction, inlet width and pressure for a small dimensionless toughness case ($\mathcal{K}_m = 0.495$). We have plotted these time evolution as function of t/t_{om} for better comparison with the LHFM solution accounting for a fluid lag (Lecampion & Detournay, 2007). For low dimensionless toughness $\mathcal{K}_m$, the response converges well to the LHFM lag solution (Lecampion & Detournay, 2007) relatively quickly after nucleation (contrary to the case of large $\mathcal{K}_m$). On Fig. 7, the convergence occurs earlier for smaller σ_o/σ_c in term of t/t_{om} - actually later for smaller σ_o/σ_c in term of $t/t_{cm} = t/t_{om} \times (\sigma_o/\sigma_c)^{-3}$ (in line with observations for larger $\mathcal{K}_m$).

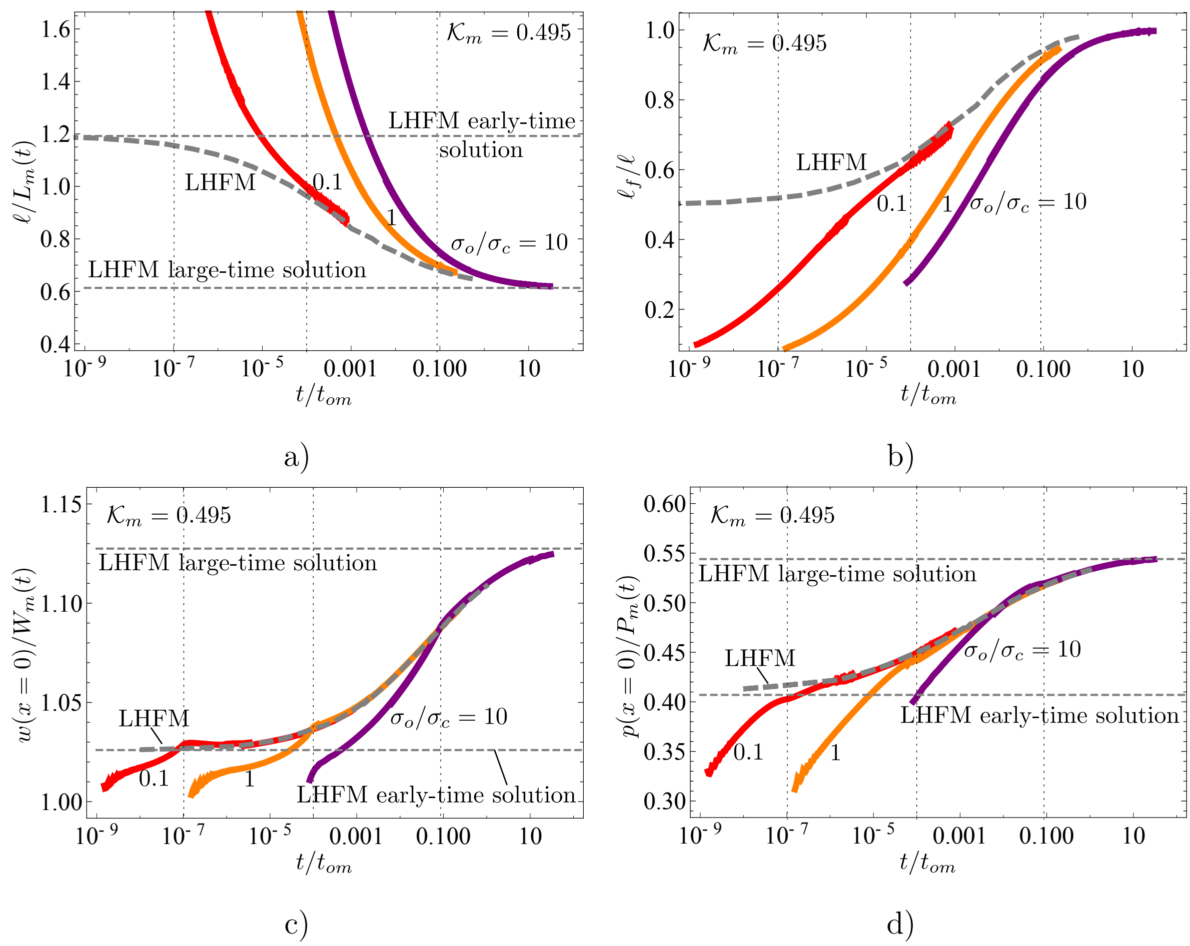

Figure 7: $\mathcal{K}_m = 0.495$: evolution of a) the fracture half length, b) fluid fraction, c) inlet width, and d) inlet net pressure with t/t_{om}. The red, orange and purple curves correspond to different confining stress $\sigma_o/\sigma_c = 0.1, 1, 10$ in a smooth cohesive HF with the dotted vertical lines as their corresponding cohesive zone nucleation period. The gray dashed curves indicate LHFM numerical results with a lag. The two gray horizontal lines correspond respectively to the LHFM early-time solutions with a lag (Garagash, 2006) and large-time solutions without a lag (Garagash & Detournay, 2005). The time evolution of the cohesive zone length and the ratio between the lag and cohesive zone sizes, fracture apparent energy and ratio of energy dissipation in viscous flow to that in fracture surface creation is shown in Supplemental Materials.

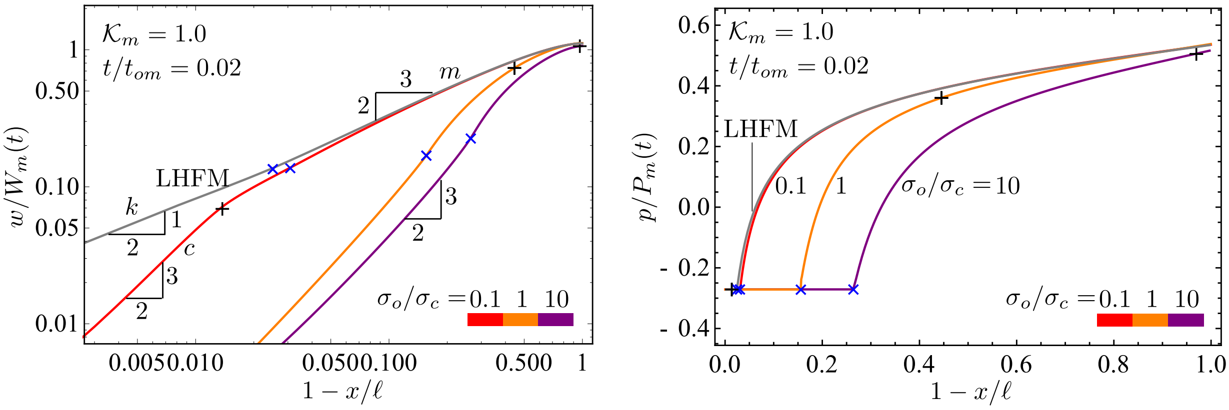

a) b)

Figure 8: a) Dimensionless opening, and b) net pressure profiles at $t/t_{om} = 0.02$ for $\mathcal{K}_m = 1.009$. "+" indicates the boundary of the cohesive zone and "×" indicates the fluid front location. The red, orange, and purple curves represent different confining stress level $\sigma_o/\sigma_c = 0.1, 1.0, 10$. The gray curves represent the LHFM solutions with a lag at the same time $t/t_{om} = 0.02$.

Tip asymptotes. The width and net pressure profiles in the tip reference frame for $\mathcal{K}_m = 1$ is displayed on Fig. 8 at time $t/t_{om} = 0.02$ for different σ_o/σ_c (thus at different t/t_{cm} for the different σ_o/σ_c and different ratio ℓ_{coh}/ℓ). On can observe different asymptotic behavior as function of distance from the tip on Fig. 8. In the far-field, the 2/3 viscosity 'm' asymptote (Desroches et al., 1994) is visible in the low confinement case - for which at this time, the fluid front is actually outside the cohesive zone. Closer to the tip, the 3/2 cohesive zone 'c' asymptote is visible. These results are in line with the cohesive tip solution of Garagash (2019), although here the cohesive zone is not necessarily small compared to the overall fracture length. This induces a significant offset compared to the semi-infinite results reported in Garagash (2019) (see Supplemental Materials for details).

5.2. A rough cohesive fracture ($\alpha_e = 2$)

The additional resistance to fluid flow associated with fracture aperture roughness has a profound impact on growth both at the nucleation and intermediate stage. The effect is amplified for larger σ_o/σ_c and larger $\mathcal{K}_m$. This can be well observed from the evolution of length, inlet width and net pressures displayed on Figures 9, 10 and 11 respectively.

In particular the net pressure and width are significantly larger compared to the smooth cohesive zone and LHFM cases, while the dimensionless length is shorter after nucleation.

The convergence toward the LHFM solutions with zero lag are in some cases not fully achieved even at very large time ($t \gg t_{cm}$ especially for the large σ_o/σ_c cases. As mentioned earlier, we actually stop these simulations when the fluid fraction $\xi_f = \ell_f/\ell$ reached 0.99 or the fracture length was within five percent of the LHFM solutions.

Faster nucleation of the cohesive zone. As the fluid front is necessarily embedded in the cohesive zone during the nucleation stage, the effect of roughness is significant during nucleation. For the same stress ratio σ_o/σ_c and dimensionless toughness $\mathcal{K}_m$, roughness influences the fracture growth by decreasing the fluid front penetration into the cohesive zone as illustrated by the evolution of the ratio between the lag and cohesive zone sizes in Fig. 13.

The increase of the fluid flow resistance brought by roughness can also be observed on the net pressure and width profiles (see Fig. 14). The steeper pressure gradient near the fluid front results in a wider opening in the fluid-filled part of the fracture, ultimately making it easier to completely debond the cohesive tractions ($w > w_c$) near the tip. The nucleation process is therefore accelerated as shown in Figs. 15, 16. The cohesive length is shorter at nucleation compared to the smooth case, but tends to converge to the same value as the smooth case at late time at least for smaller dimensionless toughness. In spite of the lack of stabilized cohesive zone length for the large dimensionless toughness / large σ_o/σ_c cases, the trend for $\sigma_o/\sigma_c = 1$ hints a similar behavior for larger confinement albeit at a much later dimensionless time.

Additional energy dissipation. These observations indicate an increase of the overall energy dissipated in the hydraulic fracturing process in the rough cohesive zone case. As shown in Figs. 16, 17, the extra energy dissipation comes from viscous fluid flow inside the rough cohesive zone and not from additional energy requirement to create new fracture surfaces. The evolution $G_{c,app}$ is not fundamentally different, with actually a smaller maximum at nucleation compared to the smooth cohesive zone case (Fig. 16). The ratio D_v/D_k of the energies dissipated in fluid viscous flow and in the creation of new fracture surfaces is significantly larger than the smooth and LHFM cases in the nucleation and intermediate stages (Fig. 17), especially for larger σ_o/σ_c. However, the D_v/D_k ratio converges toward the LHFM limit at very large time ($t \gg t_{cm}$).

Fracture aperture roughness has an impact on the fracture growth only when the fluid front is located within the cohesive zone ($\ell - \ell_f < \ell_{coh}$). For small dimensionless toughness and stress ratio, the fluid lag is larger or just slightly smaller than the cohesive zone length after nucleation (see for example the $\mathcal{K}_m = 1, \sigma_o/\sigma_c = 0.1$ case). As a result roughness has little effect and the growth is similar to the smooth case in the intermediate stage of growth. A larger dimensionless confining stress level or/and larger dimensionless toughness facilitates the penetration of the fluid front into the cohesive zone and results in additional fluid viscous dissipation due to the roughness.

At large time, the cohesive zone and fluid lag size becomes much smaller than the overall fracture length such that the effect of roughness on growth is significantly reduced. The large time trend for $\sigma_o/\sigma_c = 1$ (for all toughness) both in terms of length, width, pressure (see Figs. 9, 10, 11) as well as energy (Figs. 16) hints that the growth of a rough cohesive fracture tends to LHFM limits at sufficiently large time, similarly than for the smooth case. However, the time at which fracture growth finally follows the LHFM prediction appears much larger than t_{cm} especially for larger $\mathcal{K}_m$ and σ_o/σ_c.

6. Discussions

6.1. Implications for HF at laboratory and field scales

To gauge the implications for real systems, we consider typical values relevant to laboratory and field scales hydraulic fractures in oil/gas bearing shale/mudstone formation. These rocks have a large range of reported tensile strength ($2 - 12$ MPa - Rybacki et al. (2015)), elastic modulus ($4 - 30$ GPa - Rybacki et al. (2015)) and fracture toughness (0.18-1.43 MPa.m$^{1/2}$ - Chandler et al. (2016)). We assume in what follows $\sigma_c = 3$ MPa, $G_c = 45$ N/m, $w_c = 30\mu$m and $E' = 30$ GPa. We report the corresponding characteristic scales and dimensionless numbers for different type of injection in Table. 3.

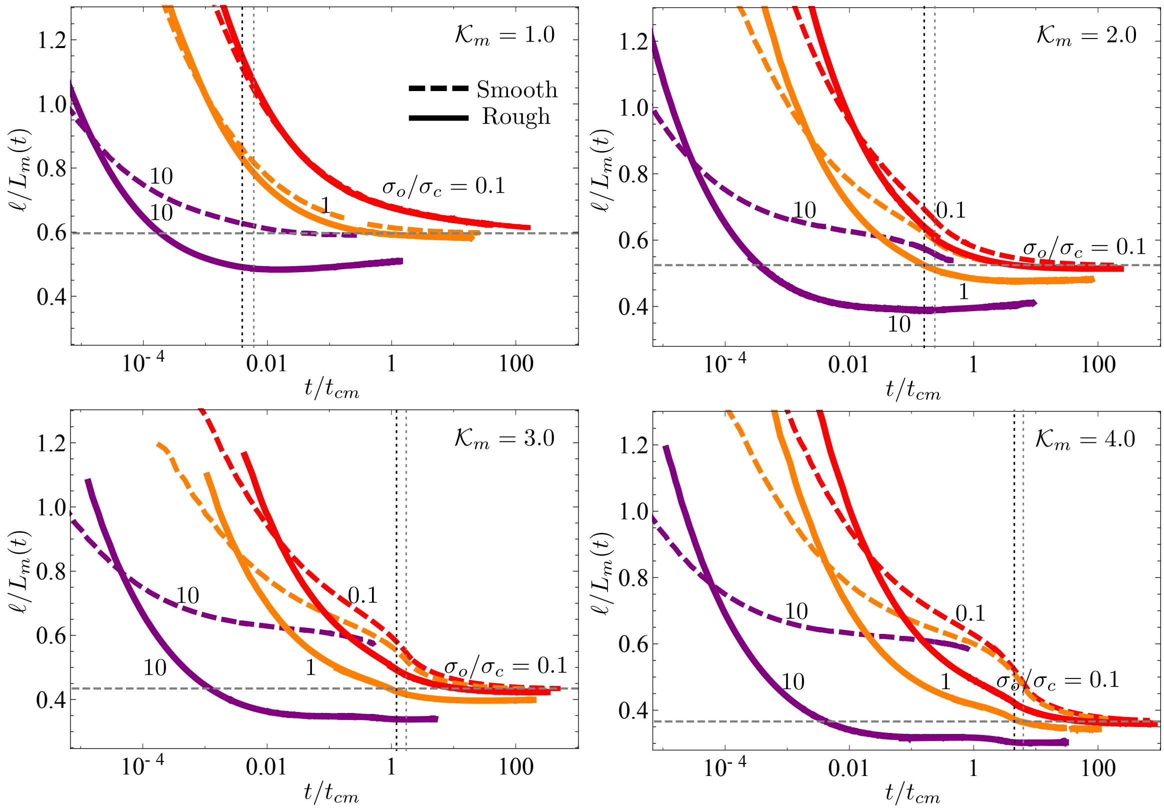

Figure 9: Evolution of the dimensionless fracture half length $\ell/L_m(t)$ with t/t_{cm} for $\mathcal{K}_m = 1 - 4$. The red, orange, and purple curves correspond respectively to $\sigma_o/\sigma_c = 0.1, 1.0, 10$ and the solid and dashed curves correspond respectively to a rough ($\alpha_e = 2$) and smooth fracture ($\alpha_e = 0$). The dotted vertical lines indicate the cohesive zone nucleation period of $\sigma_o/\sigma_c = 0.1$ for a smooth (gray) and a rough (black) fracture. The gray horizontal lines indicate the LHFM solutions in the zero fluid lag limit.

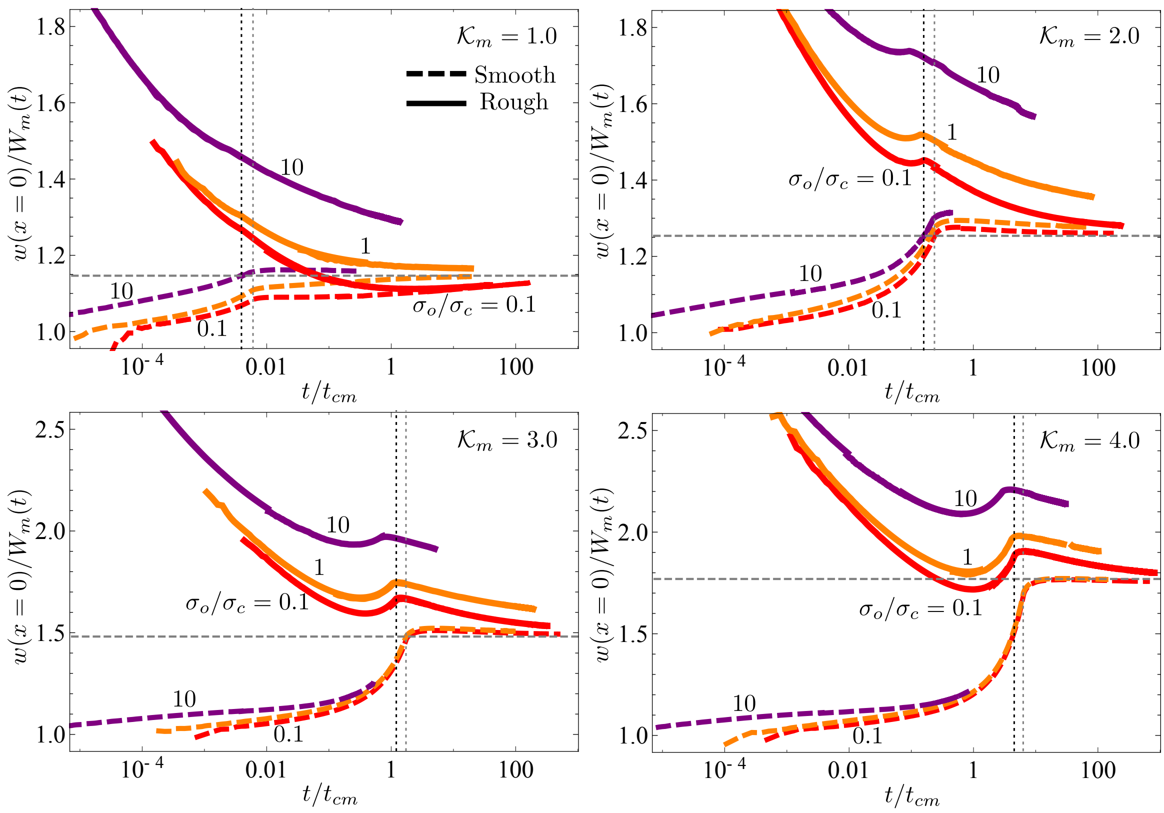

Figure 10: Evolution of the inlet width $w(x = 0)/W_m(t)$ with dimensionless time t/t_{cm} for $\mathcal{K}_m = 1 - 4$. The red, orange, and purple curves correspond respectively to $\sigma_o/\sigma_c = 0.1, 1.0, 10$ and the solid and dashed curves correspond respectively to a rough ($\alpha_e = 2$) and smooth fracture ($\alpha_e = 0$). The dotted vertical lines indicate the cohesive zone nucleation period of $\sigma_o/\sigma_c = 0.1$ for a smooth (gray) and a rough (black) fracture. The gray horizontal lines indicate the LHFM solutions in the zero fluid lag limit.

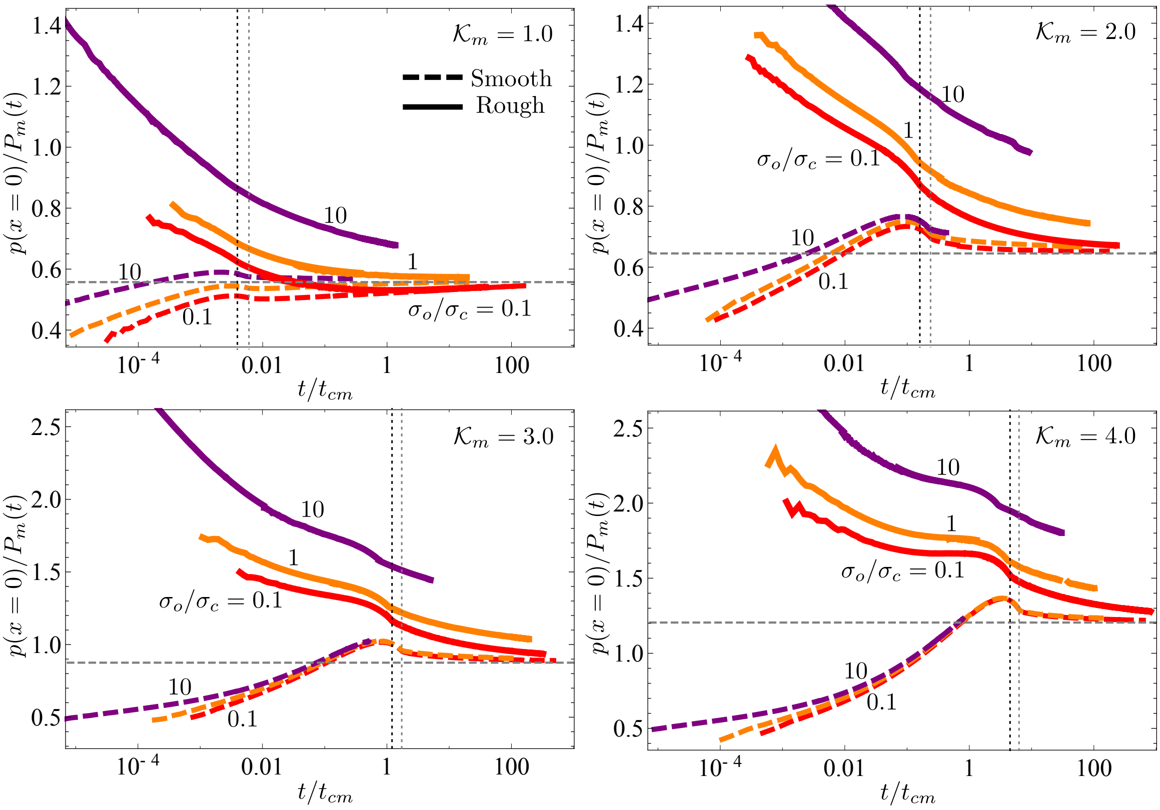

Figure 11: Evolution of the inlet net pressure $p(x=0)/P_m(t)$ with t/t_{cm} for $\mathcal{K}_m = 1-4$. The red, orange, and purple curves correspond respectively to $\sigma_o/\sigma_c = 0.1, 1.0, 10$ and the solid and dashed curves correspond respectively to a rough ($\alpha_e = 2$) and smooth fracture. The dotted vertical lines indicate the cohesive zone nucleation period of $\sigma_o/\sigma_c = 0.1$ for a smooth (gray) and a rough (black) fracture. The gray horizontal lines indicate the LHFM solutions in the zero fluid lag limit.

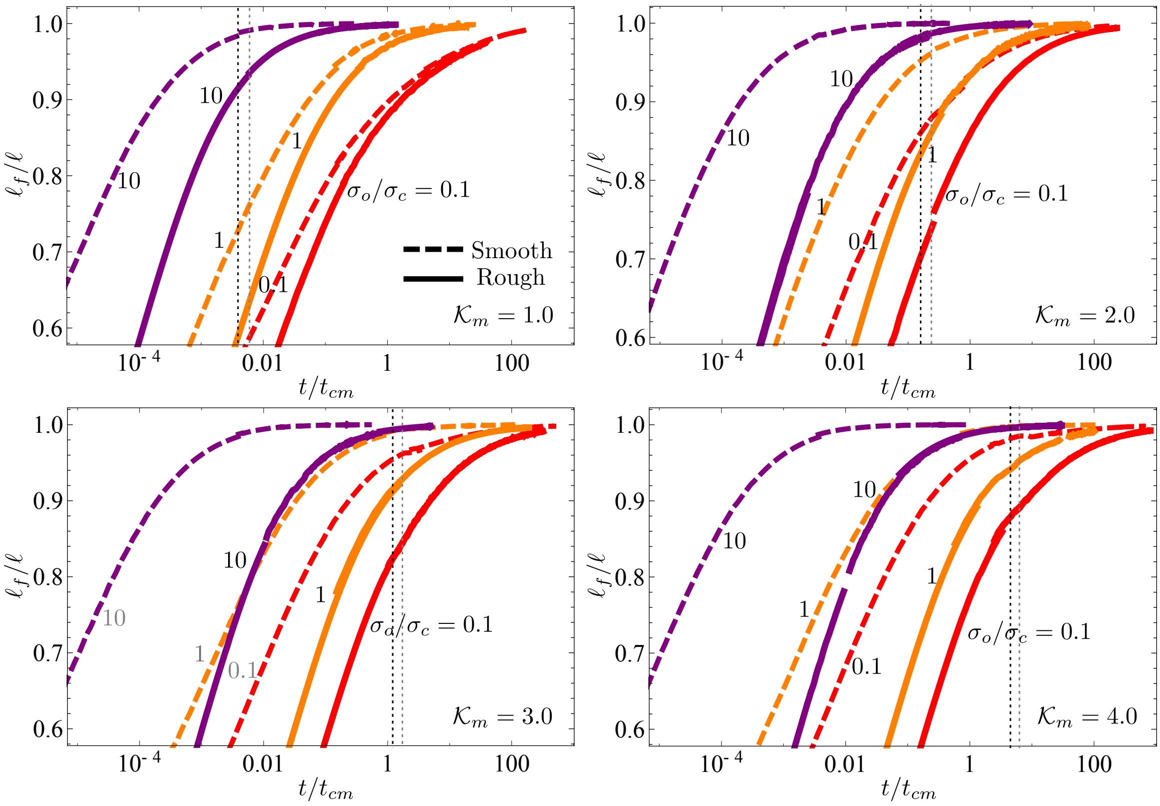

Figure 12: Evolution of the fluid fraction $\xi_f = \ell_f/\ell$ with t/t_{cm} for $\mathcal{K}_m = 1-4$. The red, orange, purple curves correspond to $\sigma_o/\sigma_c = 0.1, 1.0, 10$ and the solid and dashed curves correspond respectively to a rough ($\alpha_e = 2$) and smooth fracture ($\alpha_e = 0$). The dotted vertical lines indicate the cohesive zone nucleation period of $\sigma_o/\sigma_c = 0.1$ for a smooth (gray) and a rough (black) fracture.

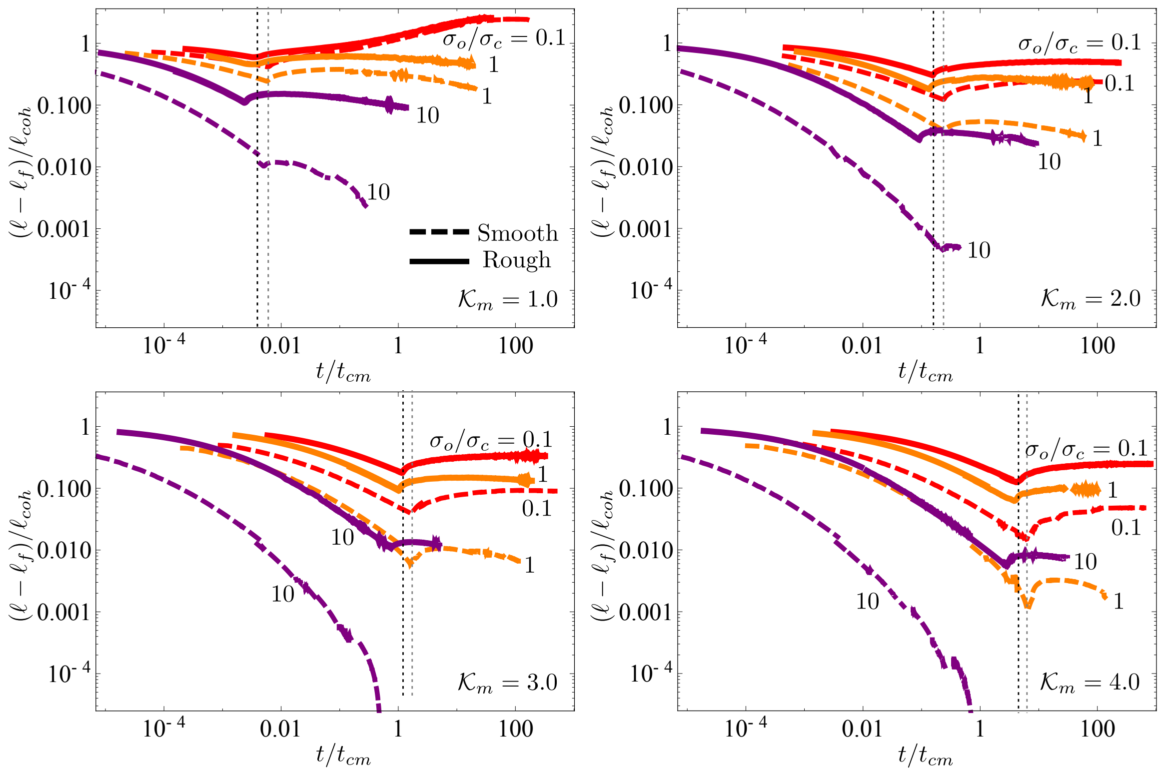

Figure 13: Time evolution of the ratio between the lag and cohesive zone sizes $(\ell - \ell_f)/\ell_{coh}$ for $\mathcal{K}_m = 1 - 4$. The red, orange, and purple curves correspond to $\sigma_o/\sigma_c = 0.1, 1.0, 10$ respectively and the solid and dashed curves correspond respectively to a rough ($\alpha_e = 2$) and smooth fracture ($\alpha_e = 0$). The dotted vertical lines indicate the cohesive zone nucleation period of $\sigma_o/\sigma_c = 0.1$ for a smooth (gray) and a rough (black) fracture.

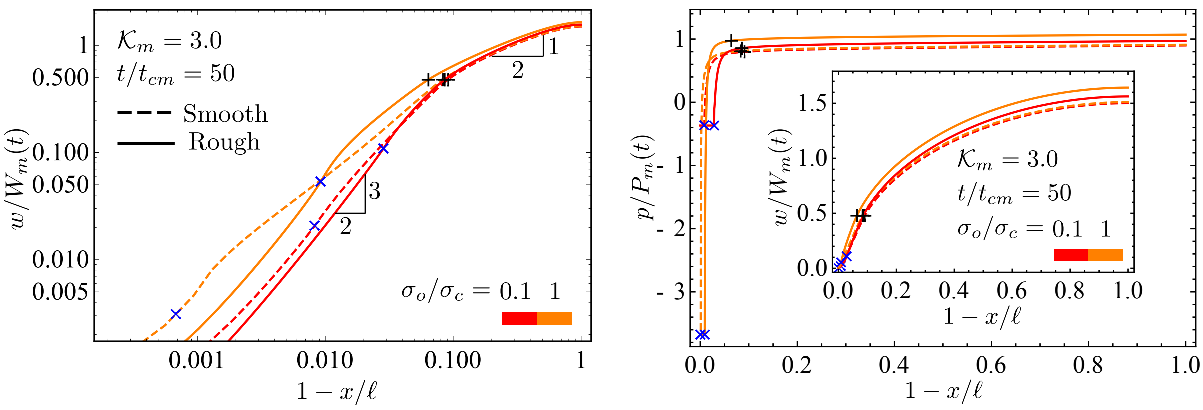

(a) (b)

Figure 14: a) Dimensionless opening and b) net pressure profiles at $t/t_{cm} = 50$ for $\mathcal{K}_m = 3.0$. "+" indicates the boundary of the cohesive zone and "×" indicates the fluid front location. The red and orange curves correspond to $\sigma_o/\sigma_c = 0.1, 1.0$ respectively. The solid and dashed curves indicate respectively a rough ($\alpha_e = 2$) and smooth fracture ($\alpha_e = 0$).

	Fracturing fluid	μ' (Pa.s)	Q_o (m^2/s)	σ_o	Injection duration (s)
Lab injection (1)	Silicone oil	12×1000	1.0×10^{-9}	3	600-1800
Lab injection (2)	Glycerol	12×0.6	1.0×10^{-9}	0.3	30-1800
Micro-HF test	Slick water	12×0.005	1.0×10^{-5}	30	60-240
Well stimulation	Slick water	12×0.005	1.0×10^{-3}	30	1800-7200
	$\mathcal{K}_m$	σ_o/σ_c	t_{cm} (s)	t_c (s)	L_{coh} (m)
Lab injection (1)	0.88	1.0	4.0×10^5	$\approx 1.6 \times 10^3$	0.3
Lab injection (2)	5.6	0.1	2.4×10^2	$> 1.1 \times 10^3$	0.3
Micro-HF test	1.8	10	2.0	≈ 0.19	0.3
Well stimulation	0.6	10	2.0	$< 4.9 \times 10^{-3}$	0.3

Table 3: Examples of characteristic scales for laboratory and field scale HF injection. We report the corresponding time t_c and length scale L_{coh} for nucleation in the rough cohesive zone case ($\alpha_e = 2$).

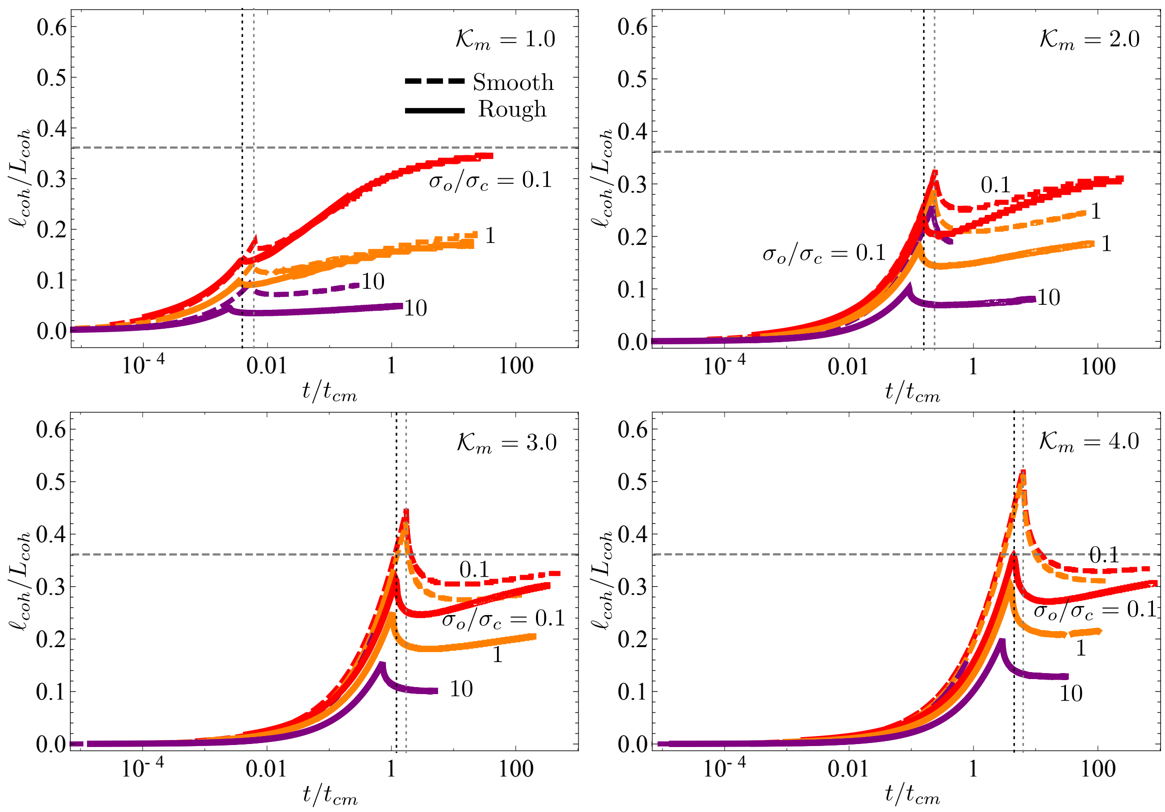

Figure 15: Time evolution of the cohesive length ℓ_{coh}/L_{coh} for $\mathcal{K}_m = 1 - 4$. The red, orange, and purple curves correspond respectively to $\sigma_o/\sigma_c = 0.1, 1.0, 10$ and the solid and dashed curves correspond respectively to a rough ($\alpha_e = 2$) and smooth fracture ($\alpha_e = 0$). The dotted vertical lines indicate the cohesive zone nucleation period of $\sigma_o/\sigma_c = 0.1$ for a smooth (gray) and a rough (black) fracture. The dashed horizontal line represents the small-scale yielding asymptote ($\approx 0.115\pi$) of the cohesive zone length for the linear-softening cohesive model (Dempsey et al., 2010).

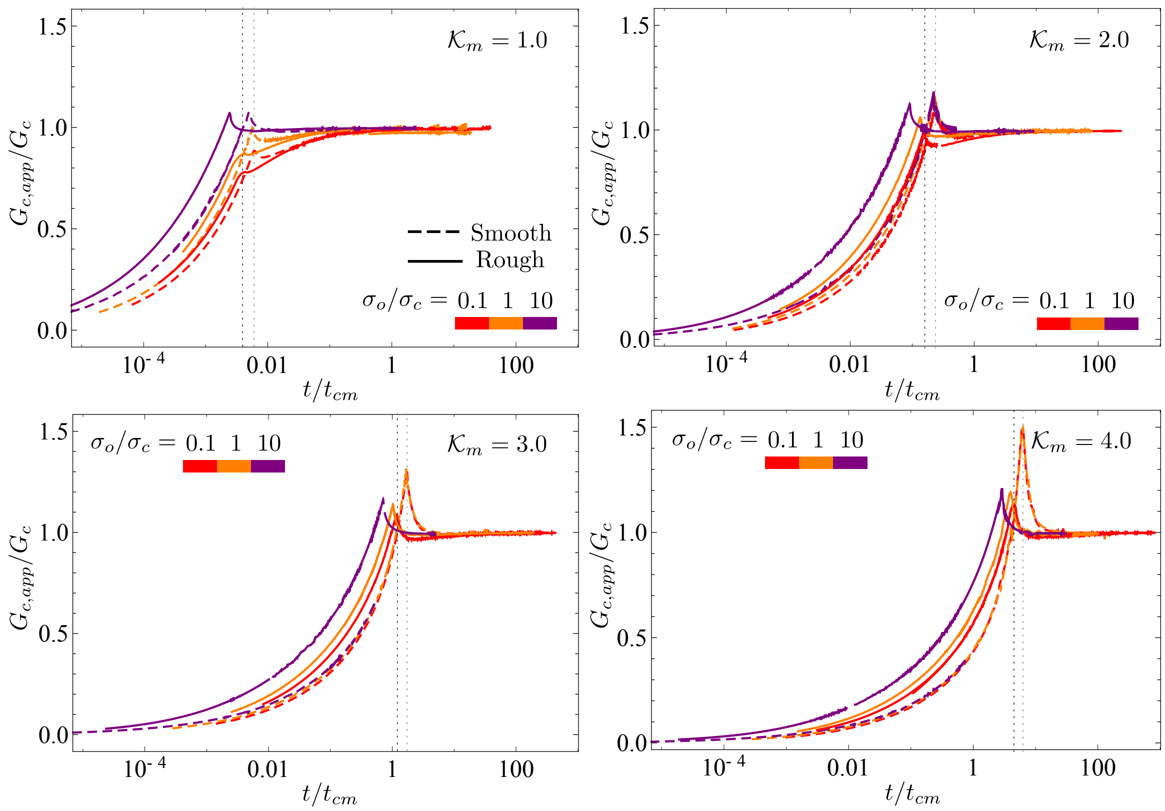

Figure 16: Time evolution of the apparent fracture energy $G_{c,app}/G_c$ for $\mathcal{K}_m = 1-4$. The red, orange, and purple curves correspond respectively to $\sigma_o/\sigma_c = 0.1, 1.0, 10$ and the solid and dashed curves correspond respectively to a rough ($\alpha_e = 2$) and smooth fracture ($\alpha_e = 0$). The dotted vertical lines indicate the cohesive zone nucleation period of $\sigma_o/\sigma_c = 0.1$ for a smooth (gray) and a rough (black) fracture.

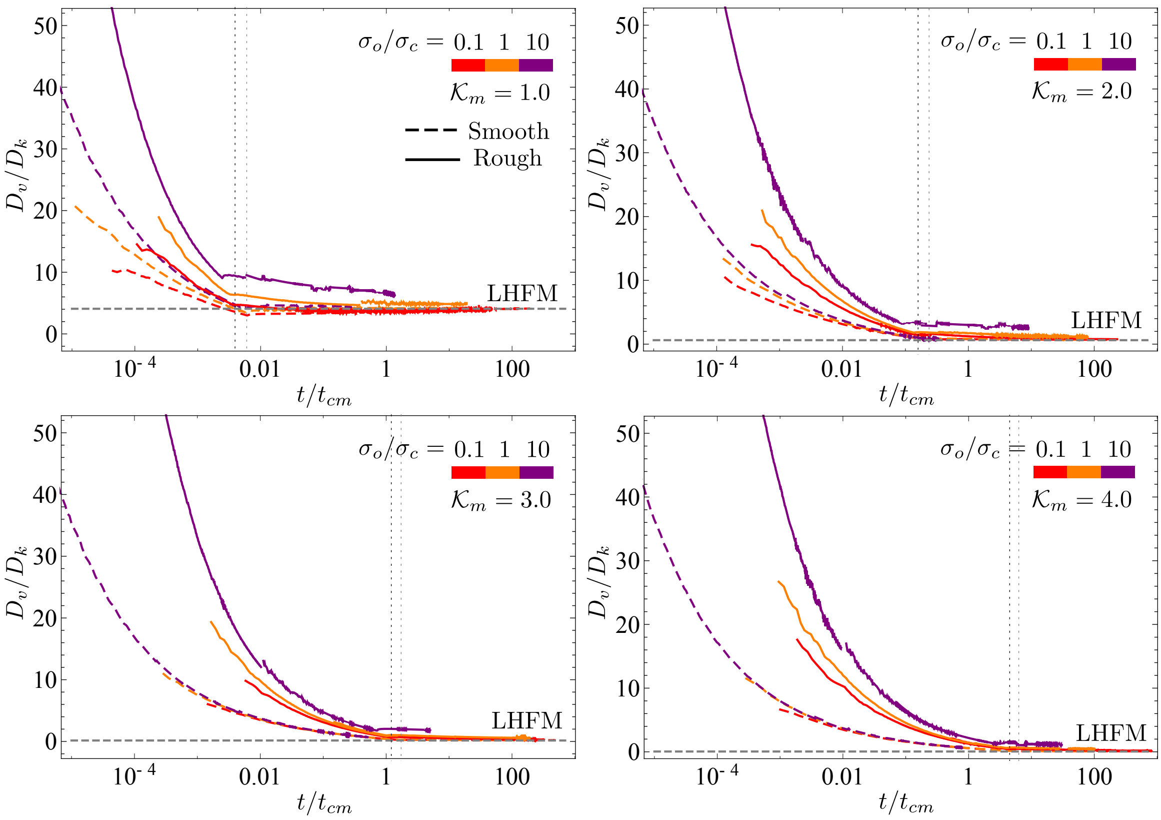

Figure 17: Time evolution of the ratio of the energies dissipated in fluid viscous flow and in the creation of new fracture surfaces D_v/D_k for $\mathcal{K}_m = 1-4$. The red, orange, and purple curves correspond respectively to $\sigma_o/\sigma_c = 0.1, 1.0, 10$ and the solid and dashed curves correspond respectively to a rough ($\alpha_e = 2$) and smooth fracture ($\alpha_e = 0$). The dotted vertical lines indicate the cohesive zone nucleation period of $\sigma_o/\sigma_c = 0.1$ for a smooth (gray) and a rough (black) fracture. The gray horizontal lines are the corresponding LHFM limits with zero fluid lag.

Laboratory HF tests are performed on finite size samples L_s (typically with L_s at most half a meter) with a minimum confining stresses either smaller or on par with the material cohesive stress ($\sigma_o/\sigma_c \approx 0.1-2$). In the case where the sample dimension L_s is smaller or of the order of the characteristic scale of the cohesive zone L_{coh}, laboratory HF tests will only span the nucleation and intermediate stages of growth, and as a result will strongly deviate from LHFM predictions. If L_s is sufficiently larger than L_{coh} ($L_s \gtrsim 10L_{coh}$), the fracture growth will possibly converge to LHFM solutions at late time for small $\mathcal{K}_m$ (Lab injection (1) case in Table. 3). Nevertheless, it will still present significant deviations from LHFM solutions in the inlet width and net pressure (see Figs. 10, 11) for larger $\mathcal{K}_m$ values (Lab injection (2) case in Table. 3).

In-situ HF operations are performed at depth (anything from 1.5 to 4 km), and as a result the ratio σ_o/σ_c is always much larger than unity ($\sigma_o/\sigma_c \sim 10$ or even larger). We evaluate the characteristic scales by assuming injection of slick water in micro-HF tests and well stimulation operations (see Table. 3). A micro-HF test (typically performed at a small injection rate) is characterized by a dimensionless toughness $\mathcal{K}_m$ around two. Based on the results presented previously, significant deviations from LHFM predictions are expected in that case with a fracture length shorter by about 15% (see Fig. 9), a fracture opening larger by about 20% (Fig. 10), and a net pressure larger by about 40% (Fig. 11) after less than a minute of propagation ($t \sim 100t_{cm}$). For well stimulation applications, the fracture growth will converge toward the LHFM predictions after few minutes thanks to the smaller dimensionless toughness resulting from the larger injection rate. This convergence will be delayed for deeper injections / larger σ_o/σ_c. One should bare in mind that very different responses can be encountered as function of rocks properties (notably of w_c, σ_c) and in-situ stress conditions.

6.2. Limitations and possible extensions of the current study

We have used a simple linear-weakening cohesive zone model to simulate the fracture process zone and a phenomenological correction to Poiseuille's law (assuming $w_R = w_c$) to account for the effect of aperture roughness on fracture hydraulic conductivity. These choices are actually the simplest possible ones, and may well be oversimplified. More advanced traction-separation relations with both a non-linear hardening and softening branch are often found to better reproduce experimental observations of fracture growth in quasi-brittle materials (Park & Paulino, 2011; Needleman, 2014). Similarly, the precise relation between the width scale of solid non-linearity w_c and that of the one related to the flow deviation w_R remains to be better constrained from experiments. A better description of the details of both the traction-separation law and the effect of roughness on fluid flow will likely modify quantitatively the hydraulic fracturing growth at the early and intermediate stages. However, the scaling and qualitative structure of HF growth presented here will remain similar. We also have to recall that a difference between w_c and w_R, or similarly a value of α_c different than unity is clearly possible in view of the scatter of the available experimental data (Table 1). This would add another dimensionless parameter (α_c) in addition to σ_o/σ_c, α_e and the dimensionless toughness $\mathcal{K}_m$.

Our results indicate a convergence of HF growth in quasi-brittle materials toward LHFM predictions at large time, even though the investigation of the parametric space reported here is only partial due to the extremely significant numerical cost of the simulation in the vanishing lag size limits as time increases. The numerical difficulty results from the requirement of a sufficiently fine mesh to resolve the shrinking fluid lag at large time as well as the small tensile zone ahead of the tip which significantly decreases for large σ_o/σ_c. An algorithm with an adaptive mesh refinement must be developed to ensure a sufficiently fine resolution of the process zone and fluid lag in order to further investigate fracture growth for large σ_o/σ_c cases.

We have assumed the flow to be strictly laminar in the rough fracture. In some specific cases where very large injection rates are used, turbulence may appear in the fracture (Lecampion & Zia, 2019; Zia & Lecampion, 2017; Dontsov, 2016). Interestingly, the deviation from smooth laminar flow via the introduction of a friction correction bears similarity with the case where turbulent flow is accounted for (Tsai & Rice, 2010; Lecampion & Zia, 2019). The impact of turbulent flow in fractures is also captured via a friction correction albeit with a different functional form. The effect of turbulence has been shown to be restricted to the early time of fracture growth (Lecampion & Zia, 2019). As such it may possibly influence the nucleation and intermediate phases of growth previously discussed for large injection rate field conditions.

The discussions and results presented here pertain to a plane-strain geometry, but can be extended to a radial hydraulic fracture (Liu & Lecampion, 2019a; Garagash, 2019). For a radial cohesive HF, the energy dissipated in the creation of fracture surfaces increases with the fracture perimeter. In particular, the dimensionless toughness $\mathcal{K}_m$ increases with time as $\mathcal{K}_m = (t/t_{mk})^{1/9}$ (Savitski & Detournay, 2002), with

$$t_{mk} = \frac{E'^{13/2} Q_o^{3/2} \mu'^{5/2}}{K'^9} \tag{32}$$

This introduces another time-scale into the problem besides t_{om} and $t_{cm} = t_{om} \times (\sigma_o/\sigma_c)^3$. As a result, the exact growth of a radial cohesive HF will be impacted by the ratio t_{cm}/t_{mk}, or in other words by the competition between hydro-mechanical effects associated with nucleation and the overall transition toward the late-time toughness dominated regime. The results of Garagash (2019) obtained using an equation of motion based on the solution of a steadily moving HF provides an estimate of the propagation, but should be taken with caution as this approach does not necessarily ensure that the cohesive zone length is smaller than the fracture length. Additional quantitative investigation of the radial cohesive HF are left for further studies.

7. Conclusions

We have investigated the growth of a plane-strain HF in a quasi-brittle material using a cohesive zone model including the effect of aperture roughness on fluid flow in the simplest possible manner. In parallel to the cohesive zone, it is necessary to account for the presence of a fluid lag to ensure that both the fluid pressure and stresses in the near tip region remain finite. Resolving with sufficient accuracy these potentially small regions near the fracture tip renders the problem extremely challenging numerically.

We have shown that a plane-strain cohesive HF presents three distinct stages of growth: a nucleation phase, an intermediate phase during which the results slowly converge toward linear hydraulic fracture mechanics (LHFM) predictions in a third stage. The overall solution is characterized by a cohesive zone nucleation time scale $t_{cm} = E'^2\mu'/\sigma_c^3$, a dimensionless fracture toughness $\mathcal{K}_m$ (whose definition is similar to the LHFM case) and the ratio between in-situ and material cohesive stress σ_o/σ_c. In addition, the enhanced flow dissipation associated with fracture roughness significantly influences the solution as it re-inforces the hydro-mechanical coupling in the near tip region.

After the nucleation stage, for large $\mathcal{K}_m$, the effect of σ_o/σ_c for a smooth cohesive zone case is not significant when the solutions tend toward the LHFM predictions. This convergence toward LHFM occurs at later t/t_{cm} for larger $\mathcal{K}_m$. For small $\mathcal{K}_m$, the fluid lag diminishes faster for larger σ_o/σ_c and the convergence to LHFM occurs for smaller t/t_{cm} as a result.

Roughness significantly modifies the convergence toward LHFM notably for dimensionless toughness larger than 1. In addition, for these large toughness cases, larger σ_o/σ_c results in larger deviations and a much slower convergence toward the LHFM predictions (which now occur for orders of magnitude of the nucleation time scale t_{cm}). Fracture roughness leads to additional energy dissipation in the viscous fluid flow associated with the fluid penetration in the cohesive zone. This ultimately results in larger openings, larger net pressures, shorter fracture extension and thus larger input energy. This additional viscous dissipation is further amplified for larger σ_o/σ_c, which facilitates the penetration of the fluid in the rough cohesive zone. It is also worth noting that counter-intuitively the effect is stronger and remains in effect longer for larger dimensionless toughness: the viscous pressure drop localizes to an even smaller region near the tip for larger $\mathcal{K}_m$ such that viscous flow dissipation increases as a result.

Different models for the impact of roughness on flow (such as different values for α_c and the power-law flow roughness exponent α_e taken here equal to 1 and 2 respectively) will impact quantitatively the fracture evolution although the structure of the solution described here will remain. The same can be said with regards to the simple linear-weakening traction separation law used which may be replaced by a more elaborate one if required.

The theoretical predictions presented here need to be tested experimentally on well characterized quasi-brittle materials. This is particularly challenging as one must ensure that the sample size is at least ten times larger than the characteristic cohesive zone length $L_{coh} = E' w_c / \sigma_c$ in order to hope capturing the convergence toward LHFM predictions. It is actually worth noting that so far all the quantitative experimental validations of linear hydraulic fracture mechanics have been obtained on transparent and/or model materials - all with very small process zone sizes (see Lecampion et al. (2017) and references therein). HF experiments in rocks need to performed with a quantitative measurement of the time evolution of the fracture and fluid fronts, as well as fracture opening. This is achievable via active acoustic imaging (Liu et al., 2020). However, the accurate spatiotemporal imaging of the process zone of a growing hydraulic fracture under realistic stress and injection conditions remains truly challenging.

Acknowledgement

The authors would like to thank Dmitry I. Garagash for insightful discussions at the early stage of this research.

CRediT Authors contributions

Dong Liu: Conceptualization, Methodology, Formal analysis, Software, Investigation, Validation, Visualization, Writing – original draft.

Brice Lecampion: Conceptualization, Methodology, Supervision, Writing – review & editing.

Appendix A. Numerical scheme accounting for the nucleation of a cohesive zone and a fluid lag

As suggested in Liu & Lecampion (2019b), the problem is solved numerically via a fully implicit scheme based on the boundary element method. We automatically nucleate the fluid lag using the Elrod-Adams lubrication cavitation model at the early stage of fracture growth (Mollaali & Shen, 2018). We then switch to a level-set algorithm for computational efficiency by precisely tracking the fluid front (Gordeliy & Detournay, 2011).

Appendix A.1. Fluid-lag-nucleation algorithm

We initiate the fracture aperture from the solution of a static elastic fracture under a uniform fluid pressure slightly larger than σ_o. For a given fracture length increment, the solution is obtained using three nested iterative loops: we start from a trial time step and solve the fluid pressure for all elements inside the fracture using a quasi-Newton method. Such a procedure is repeated until each element in the fracture reaches a consistent state: either fluid or vapor. A converged estimate of the cohesive forces is then updated using fixed-point iterations with under-relaxation. The time step is finally adjusted in an outer loop using a bi-section and secant method to fulfill the propagation criterion.

Elasticity.

$$\mathbb{A}\mathbf{w} = \mathbf{p}_f - \sigma_{coh}(\mathbf{w}) - \sigma_o \tag{A.1}$$

where $\mathbb{A}$ is the elastic matrix obtained via the discretization of the elastic operator using the displacement discontinuity method with piece-wise constant elements, and $\mathbf{p}_f, \sigma_o, \sigma_{coh}$ are respectively vectors of the fluid pressure, minimum compressive stress and cohesive forces.

Elrod-Adams lubrication. A state variable θ is introduced in the mass conservation, characterizing the percentage of liquid occupying the fracture within one element. All the elements inside the fracture fulfil the condition $p_f(1-\theta) = 0$ and can be classified into three domains according to the filling condition of the element: η_p (elements fully filled with fluid), η_θ (elements partially filled with fluid) and η_{ex} (empty or vapor elements).

$$\begin{aligned} \eta_p &= \{i \in \eta_\Gamma \mid \theta_i = 1, \quad p_{fi} > 0\} \\ \eta_\theta &= \{i \in \eta_\Gamma \mid 0 < \theta_i < 1, \quad p_{fi} = 0\} \\ \eta_{ex} &= \{i \in \eta_\Gamma \mid i \notin (\eta_p \cup \eta_\theta), \quad p_{fi} = 0, \quad \theta_i = 0\} \end{aligned} \tag{A.2}$$

where $\eta_p \cap \eta_\theta = \emptyset$ and $\eta_\Gamma = \eta_p \cup \eta_\theta \cup \eta_{ex}$. We integrate the lubrication equation over element i:

$$\underbrace{\int_i \frac{\partial(\theta w)}{\partial t}\mathrm{d}x}_{1} + \underbrace{\int_i \frac{\partial}{\partial x}\left(-\frac{w^3}{\mu'}\frac{\partial p_f}{\partial x}\right)\mathrm{d}x}_{2} - \underbrace{\frac{Q_o}{2}\delta_{(i,1)}}_{3} = 0 \tag{A.3}$$

Repeat solving for pressure p_{fi}, θ_i for $i \in \eta_p \cup \eta_\theta$ using Newton's method;

  for $i \in \eta_\Gamma$ **do**

    if $p_{f,i} < 0$ **then** set $p_{f,i} = 0$, $\eta_p \leftarrow \eta_p \setminus \{i\}$, $\eta_\theta \leftarrow \eta_\theta \cup \{i\}$, $\eta_{ex} \leftarrow \eta_\Gamma \setminus (\eta_p \cup \eta_\theta)$

    if $\theta_i > 1$ **then** set $\theta_i = 1$, $\eta_\theta \leftarrow \eta_\theta \setminus \{i\}$, $\eta_p \leftarrow \eta_p \cup \{i\}$, $\eta_{ex} \leftarrow \eta_\Gamma \setminus (\eta_p \cup \eta_\theta)$

    if $\theta_i < 0$ **then** set $\theta_i = 0$, $\eta_\theta \leftarrow \eta_\theta \setminus \{i\}$, $\eta_{ex} \leftarrow \eta_\Gamma \setminus (\eta_p \cup \eta_\theta)$

  end

until all constraints $p_{f,i} \geq 0$, $0 \leq \theta_i \leq 1$ for $i \in \eta_\Gamma$ are satisfied, in other words, $p_{f,i}(1-\theta_i) = 0$.

Table A.4: Algorithm using the Elrod-Adams model (adapted from Mollaali & Shen (2018)) within one iteration with a given cohesive force vector

The first and the second terms are respectively discretized as follows,

$$\int_i \frac{\partial \theta w}{\partial t} \mathrm{d}x = \frac{1}{\Delta t} h(\theta_i w_i - \theta_i^o w_i^o) \tag{A.4}$$

$$\begin{aligned} &\int_i \frac{\partial}{\partial x}\left(-\frac{w^3}{\mu' f}\frac{\partial p_f}{\partial x}\right)\mathrm{d}x = \left[-\frac{w^3}{\mu' f}\frac{\partial p_f}{\partial x}\right]_{i-1/2}^{i+1/2} \\ &= \frac{1}{\mu' f_{i-1/2}} w_{i-1/2}^3 \left(\frac{p_{f,i} - p_{f,i-1}}{h}\right) - \frac{1}{\mu' f_{i+1/2}} w_{i+1/2}^3 \left(\frac{p_{f,i+1} - p_{f,i}}{h}\right), \\ &w_{i-1/2} = \frac{w_i + w_{i-1}}{2}, \quad w_{i+1/2} = \frac{w_i + w_{i+1}}{2} \end{aligned} \tag{A.5}$$

where h is the element size and the superscript o denotes the solution at the previous time step.

We back-substitute the elasticity into the lubrication equation and use the quasi-Newton method to solve the non-linear problem. We set the solution of the previous time step as an initial guess and solve iteratively for $p_{f,i}(i \in \eta_p)$ and $\theta_i(i \in \eta_\theta)$. The lag-nucleation algorithm then updates the sets of η_p and η_θ as demonstrated in Table A.4.

Propagation condition. In the context of a cohesive zone, we check the equality of the tensile stress component ahead of the fracture tip with the material peak strength:

$$\sigma_{yy,n+1} = A_{n+1,j} w_j - \sigma_o = \sigma_c, \quad j = 1...n \tag{A.6}$$

where n is the number of elements inside the fracture at the current time step.

Appendix A.2. Fluid-front-tracking algorithm

The fluid-front tracking algorithm (Gordeliy & Detournay, 2011) assumes a clear boundary between the fluid and cavity. The n elements inside the fracture is divided into m fluid channel elements fully-filled with fluid ($p_f > 0$), $(n - m - 1)$ fluid lag elements with a negligible cavitation pressure ($p_f = 0$) and one partially filled element ($p_f = 0$) where locates the fluid front. By introducing a filling fraction ϕ, we estimate the fluid front position using the solution of the lag-nucleation / Elrod-Adams based algorithm. We assume that fluid-front-tracking algorithm initializes with a solution $(w^O, p_f^O, V^O, m^O, \phi^O, \ell_f^O)$ obtained from the lag-nucleation / Elrod-Adams based algorithm at a chosen time step k. m^O is the number of elements in the domain η_p. ϕ^O is the filling fraction obtained by gathering the fluid mass of all lag elements from the lag-nucleation algorithm in the partially-filled element (the $(m^O + 1)^{\text{th}}$ element) of the fluid-front-tracking algorithm.

$$\phi^O = \sum_i \theta_i^k w_i^k / w_{m^O+1}, \quad i \in \eta_\theta \tag{A.7}$$

We then obtain the fluid front position ℓ_f^O and the fluid front velocity V^O for a chosen time step k.

$$\begin{aligned} \ell_f^O &= (m^O + \phi^O)h, \\ V^O &= (\ell_{f,k+1} - \ell_{f,k-1})/(t_{k+1} - t_{k-1}) \end{aligned} \tag{A.8}$$

where and t_{k-1} and t_{k+1} are respectively propagation time at the $(k-1)^{\text{th}}$ and $(k+1)^{\text{th}}$ time step in the lag-nucleation algorithm.

Based on this initial estimation of the fluid front, we solve iteratively the increment of the opening in the channel elements for a given fracture front through three nested loops in the fluid-front-tracking algorithm. One loop tracks the fluid front, one updates the time step to fulfill the propagation condition and another solves the non-linear system due to the cohesive forces and lubricated fluid flow through a fixed-point scheme. We present in the following the discretization of the non-linear system.

Elasticity.

$$\mathbf{p}_c - \sigma_o - \sigma_{cohc} = \mathbb{A}_{cw}\mathbf{w} + \mathbb{A}_{ol}(-\sigma_o - \sigma_{cohl}) \tag{A.9}$$

where $\mathbf{p}_c$ is the vector net pressures in the channel part of the fracture; σ_{cohc} and σ_{cohl} cohesive forces applied in the fluid channel and fluid lag.

$$\begin{aligned} \mathbb{A}_{cw} &= \mathbb{A}_{cc} - \mathbb{A}_{cl}\mathbb{A}_{ll}^{-1}\mathbb{A}_{lc} \\ \mathbb{A}_{ol} &= \mathbb{A}_{cl}\mathbb{A}_{ll}^{-1} \end{aligned} \tag{A.10}$$

$\mathbb{A}_{cc}, \mathbb{A}_{cl}, \mathbb{A}_{lc}, \mathbb{A}_{ll}$ are sub-matrix of the elastic matrix $\mathbb{A}$ associated with elements inside the fluid channel and lag.

Lubrication flow. For fluid channel elements ($1 \leq i \leq m$),

$$\begin{aligned} \Delta w_i =& \frac{\Delta t}{\mu' h^2}\left(\frac{1}{f_{i-1/2}} w_{i-1/2}^3 p_{c,i-1} + \frac{1}{f_{i+1/2}} w_{i+1/2}^3 p_{c,i+1}\right) \\ & - \frac{\Delta t}{\mu' h^2}\left(\frac{1}{f_{i-1/2}} w_{i-1/2}^3 + \frac{1}{f_{i+1/2}} w_{i+1/2}^3\right) p_{c,i} + \delta_{(i,1)} \frac{Q_o \Delta t}{2h} \\ & - \delta_{(i,m)} F_m - H(i - m^o) \sum_{k=m^o+1}^{m} \delta_{(i,k)} F_k \end{aligned} \tag{A.11}$$

The second term on the second line represents the contribution due to a constant injection rate and the two terms on the third line are mass corrections due to the partially-filled element where the fluid front locates. $H(\cdot)$ is the Heaviside step function.

$$F_m = \begin{cases} \phi w_{m+1} - \phi^o w_{m+1}^o, & m = m^o \\ \phi w_{m+1} - \phi^o w_{m^o+1}^o - \sum_{i=m+1}^{m^o} w_i, & m < m^o \end{cases} \tag{A.12}$$

$$F_k = \begin{cases} (1 - \phi^o) w_k^o, & k = m^o + 1 \\ w_k^o, & k > m^o + 1 \end{cases} \tag{A.13}$$

where the superscript o refers to the solutions at the previous time step. The lubrication equation can be thus arranged as

$$\Delta \mathbf{w} = \mathbb{L} \cdot \mathbf{p}_c + \mathbf{S}_1 - \mathbf{S}_m - \mathbf{S}_{m^o} \tag{A.14}$$

Coupled system of equations. We back-substitute the elasticity and write the coupled system as in Eq. (A.15). For a given fracture front and a trial time step, we solve for incremental apertures $\Delta\mathbf{w}$ using fixed-point iterations. The tangent linear system reads:

$$(\mathbb{I} - \mathbb{L}(\Delta\mathbf{w}^{(s-1)})\mathbb{A}_{cw})\Delta\mathbf{w}^s = \mathbb{L}(\Delta\mathbf{w}^{(s-1)})\mathbb{A}_{cw}\mathbf{w}^o + \mathbb{L}(\Delta\mathbf{w}^{(s-1)})\mathbb{A}_{ol}(-\sigma_o - \sigma_{cohl}(\Delta\mathbf{w}^{(s-1)})) \tag{A.15}$$

where s refers to the solution at the previous iteration.

Update of the fluid front position. The fluid front position is estimated as

$$\ell_f^{(s)} = (m^o + \phi^o)h + V^{(s-1)}\Delta t, m^{(s)} = \text{floor}[\ell_f^{(s)}/h], \phi^{(s)} = \ell_f^{(s)}/h - m^{(s)} \tag{A.16}$$

where V is the fluid front velocity and it can be obtained through lubrication theories,

$$\begin{aligned} V &= \frac{1}{2}\left(V^o - \frac{1}{\mu' f_m} w_m^2 \frac{\partial p}{\partial x}\right), \\ \frac{\partial p}{\partial x} &= \left(p_{c,m} - \frac{p_{c,m} + \sigma_o}{\phi + 1/2} - p_{c,m-1}\right)/(2h), \quad m > 1 \end{aligned} \tag{A.17}$$

The iteration starts with $V^{(0)} = V^o$ and continues until $|(\ell_f^{(s)} - \ell_f^{(s-1)})/\ell_f^{(s-1)}|$ is within a set tolerance.

Control of overestimation of the fluid front position. We may possibly overestimate the fluid front position using Eq. (A.16) especially when the fracture front advances too much compared to the previous time step. As a result, negative pressure may be detected in the channel elements near the fluid front.

In order to better locate the fluid front, we adopt a strategy similar to the one in Gordeliy et al. (2019). Once the scheme detects a negative fluid pressure in the channel elements (where the elements are fully-filled with fluid) during the s^{th} iteration at the current time step, we utilizes the bi-section algorithm to estimate the fluid front position (Liu & Lecampion, 2019a). We set the fluid front position at the previous time step as the lower bound $\ell_{f-} = \ell_f^o$ and the current position obtained from the previous iteration as the upper bound $\ell_{f+} = \ell_f^{(s-1)}$. As long as the fluid front advances during the fracture growth, the trial fluid front position for the next iteration can be estimated from

$$\ell_f^{(s)} = (\ell_{f+} + \ell_{f-})/2 \tag{A.18}$$

We iterate on ℓ_f until that $|(\ell_f^{(s)} - \ell_f^{(s-1)})/\ell_f^{(s-1)}|$ is within a set tolerance and that all fluid pressure in the channel elements remain positive.

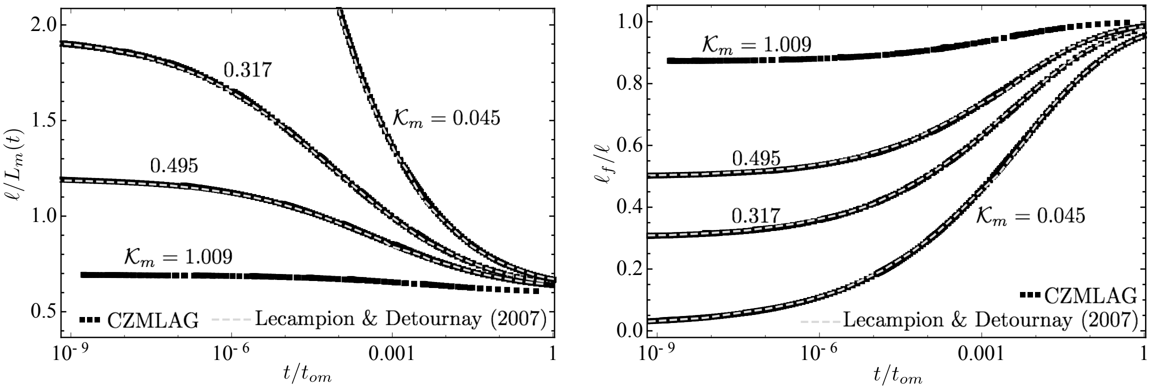

a) b)

Figure A.18: Time evolution of a) the half fracture length and b) fluid fraction in viscosity scaling for different dimensionless toughness $\mathcal{K}_m$.

Appendix A.3. Benchmark of the growth of a linear elastic fracture

We simulate the growth of a plane-strain HF in a linear elastic medium by adapting the propagation condition as

$$w_n = \frac{2}{3}\frac{K'\sqrt{h}}{E'} \tag{A.19}$$

where w_n is the opening of the element closest to the fracture tip obtained by the integration of the tip asymptote. We benchmark our scheme using different $\mathcal{K}_m$ values and formulate the problem with the viscosity scaling in the time-domain t/t_{om} similar to Lecampion & Detournay (2007). We show in Fig. A.18 that our results (CZMLAG) are in good agreement with the numerical solutions reported in Lecampion & Detournay (2007).

References

Bazant, Z. P., & Planas, J. (1997). *Fracture and size effect in concrete and other quasibrittle materials* volume 16. CRC press.

Bonamy, D., Ponson, L., Prades, S., Bouchaud, E., & Guillot, C. (2006). Scaling exponents for fracture surfaces in homogeneous glass and glassy ceramics. *Physical Review Letters*, *97*, 135504.

Breysse, D., & Gérard, B. (1997). Transport of fluids in cracked media. *Rilem report*, (pp. 123–154).

Bueckner, H. (1970). A novel principle for the computation of stress intensity factors. *Zeitschrift fuer Angewandte Mathematik & Mechanik*, *50*, 529–546.

Bunger, A. P., & Detournay, E. (2008). Experimental validation of the tip asymptotics for a fluid-driven crack. *Journal of the Mechanics and Physics of Solids*, *56*, 3101–3115.

Carrier, B., & Granet, S. (2012). Numerical modeling of hydraulic fracture problem in permeable medium using cohesive zone model. *Engineering Fracture Mechanics*, *79*, 312–328.

Chandler, M. R., Meredith, P. G., Brantut, N., & Crawford, B. R. (2016). Fracture toughness anisotropy in shale. *Journal of Geophysical Research: Solid Earth*, *121*, 1706–1729.

Chen, Z. (2012). Finite element modelling of viscosity-dominated hydraulic fractures. *Journal of Petroleum Science and Engineering*, *88*, 136–144.

Chen, Z., Bunger, A., Zhang, X., & Jeffrey, R. G. (2009). Cohesive zone finite element-based modeling of hydraulic fractures. *Acta Mechanica Solida Sinica*, *22*, 443–452.

Dempsey, J. P., Tan, L., & Wang, S. (2010). An isolated cohesive crack in tension. *Continuum Mechanics and Thermodynamics*, *22*, 617–634.

Desroches, J., Detournay, E., Lenoach, B., Papanastasiou, P., Pearson, J. R. A., Thiercelin, M., & Cheng, A. (1994). The crack tip region in hydraulic fracturing. *Proceedings of the Royal Society of London. Series A: Mathematical and Physical Sciences*, *447*, 39–48.

Detournay, E. (2004). Propagation regimes of fluid-driven fractures in impermeable rocks. *International Journal of Geomechanics*, *4*, 35–45.

Detournay, E. (2016). Mechanics of hydraulic fractures. *Annual Review of Fluid Mechanics*, *48*, 311–339.

Dontsov, E. (2016). Tip region of a hydraulic fracture driven by a laminar-to-turbulent fluid flow. *Journal of Fluid Mechanics*, *797*.

Falk, M. L., Needleman, A., & Rice, J. R. (2001). A critical evaluation of cohesive zone models of dynamic fractur. *Le Journal de Physique IV*, *11*, Pr5–43.

Garagash, D. I. (2000). Hydraulic fracture propagation in elastic rock with large toughness. In *4^{th} North American Rock Mechanics Symposium* ARMA-2000-0221. ARMA.

Garagash, D. I. (2006). Propagation of a plane-strain hydraulic fracture with a fluid lag: Early-time solution. *International Journal of Solids and Structures*, *43*, 5811 – 5835.

Garagash, D. I. (2015). How fracking can be tough. IMA Workshop Hydraulic Fracturing Modeling and Simulation to Reconstruction and Characterization, University of Minnesota.

Garagash, D. I. (2019). Cohesive-zone effects in hydraulic fracture propagation. *Journal of the Mechanics and Physics of Solids*, *133*, 103727.

Garagash, D. I., & Detournay, E. (2000). The tip region of a fluid-driven fracture in an elastic medium. *ASME Journal of Applied Mechanics*, *67*, 183–192.

Garagash, D. I., & Detournay, E. (2005). Plane-strain propagation of a fluid-driven fracture: small toughness solution. *Journal of applied mechanics*, *72*, 916–928.

Gordeliy, E., Abbas, S., & Peirce, A. (2019). Modeling nonplanar hydraulic fracture propagation using the XFEM: An implicit level-set algorithm and fracture tip asymptotics. *International Journal of Solids and Structures*, *159*, 135–155.

Gordeliy, E., & Detournay, E. (2011). A fixed grid algorithm for simulating the propagation of a shallow hydraulic fracture with a fluid lag. *International Journal for Numerical and Analytical Methods in Geomechanics*, *35*, 602–629.

Hillerborg, A., Modéer, M., & Petersson, P.-E. (1976). Analysis of crack formation and crack growth in concrete by means of fracture mechanics and finite elements. *Cement and Concrete Research*, *6*, 773–781.

Hills, D., Kelly, P., Dai, D., & Korsunsky, A. (1996). *Solution of Crack Problems: The Distributed Dislocation Technique*. Journal of Applied Mechanics. Kluwer Academic Publishers.

Jin, Y., Dong, J., Zhang, X., Li, X., & Wu, Y. (2017). Scale and size effects on fluid flow through self-affine rough fractures. *International Journal of Heat and Mass Transfer*, *105*, 443–451.

Lecampion, B. (2012). Modeling size effects associated with tensile fracture initiation from a wellbore. *International Journal of Rock Mechanics and Mining Sciences*, *56*, 67–76.

Lecampion, B., Bunger, A. P., & Zhang, X. (2018). Numerical methods for hydraulic fracture propagation: A review of recent trends. *Journal of Natural Gas Science and Engineering*, *49*, 66–83.

Lecampion, B., Desroches, J., Jeffrey, R. G., & Bunger, A. P. (2017). Experiments versus theory for the initiation and propagation of radial hydraulic fractures in low permeability materials. *Journal of Geophysical Research: Solid Earth*, *122*.

Lecampion, B., & Detournay, E. (2007). An implicit algorithm for the propagation of a hydraulic fracture with a fluid lag. *Computer Methods in Applied Mechanics and Engineering*, *196*, 4863–4880.

Lecampion, B., & Zia, H. (2019). Slickwater hydraulic fracture propagation: near-tip and radial geometry solutions. *Journal of Fluid Mechanics*, *880*, 514–550.

Lhomme, T. P. Y. (2005). *Initiation of hydraulic fractures in natural sandstones*. TU Delft, Delft University of Technology.

Li, Y., Deng, J., Liu, W., & Feng, Y. (2017). Modeling hydraulic fracture propagation using cohesive zone model equipped with frictional contact capability. *Computers and Geotechnics*, *91*, 58–70.

Liu, D., & Lecampion, B. (2019a). Growth of a radial hydraulic fracture accounting for the viscous fluid flow in a rough cohesive zone. In *ARMA-CUPB Geothermal International Conference* ARMA-CUPB-19-4210. ARMA.

Liu, D., & Lecampion, B. (2019b). Propagation of a plane-strain hydraulic fracture accounting for the presence of a cohesive zone and a fluid lag. In *53^{rd} US Rock Mechanics/Geomechanics Symposium* ARMA-2019-0103. ARMA.

Liu, D., Lecampion, B., & Blum, T. (2020). Time-lapse reconstruction of the fracture front from diffracted waves arrivals in laboratory hydraulic fracture experiments. *Geophysical Journal International*, *223*, 180–196.

Liu, D., Lecampion, B., & Garagash, D. I. (2019). Propagation of a fluid-driven fracture with fracture length dependent apparent toughness. *Engineering Fracture Mechanics*, *220*, 106616.

Lomize, G. (1951). Water flow through jointed rock. *Gosenergoizdat, Moscow*, (p. 127).

Moës, N., & Belytschko, T. (2002). Extended finite element method for cohesive crack growth. *Engineering Fracture Mechanics*, *69*, 813–833.

Mollaali, M., & Shen, Y. (2018). An Elrod–Adams-model-based method to account for the fluid lag in hydraulic fracturing in 2D and 3D. *International Journal of Fracture*, *211*, 183–202.

Morel, S., Bonamy, D., Ponson, L., & Bouchaud, E. (2008). Transient damage spreading and anomalous scaling in mortar crack surfaces. *Physics Review E*, *78*, 016112.

Mourot, G., Morel, S., Bouchaud, E., & Valentin, G. (2005). Anomalous scaling of mortar fracture surfaces. *Physics Review E*, *71*, 016136.

Needleman, A. (2014). Some issues in cohesive surface modeling. *Procedia IUTAM*, *10*, 221–246.

Papanastasiou, P. (1997). The influence of plasticity in hydraulic fracturing. *International Journal of Fracture*, *84*, 61–79.

Papanastasiou, P. (1999). The effective fracture toughness in hydraulic fracturing. *International Journal of Fracture*, *96*, 127–147.

Papanastasiou, P., & Atkinson, C. (2006). Representation of crack-tip plasticity in pressure sensitive geomaterials: Large scale yielding. *International Journal of Fracture*, *139*, 137–144.

Park, K., & Paulino, G. H. (2011). Cohesive zone models: a critical review of traction-separation relationships across fracture surfaces. *Applied Mechanics Reviews*, *64*.

Ponson, L., Auradou, H., Pessel, M., Lazarus, V., & Hulin, J.-P. (2007). Failure mechanisms and surface roughness statistics of fractured fontainebleau sandstone. *Physics Review E*, *76*, 036108.

Raven, K., & Gale, J. (1985). Water flow in a natural rock fracture as a function of stress and sample size. *International Journal of Rock Mechanics and Mining Sciences & Geomechanics Abstracts*, *22*, 251–261.

Renshaw, C. E. (1995). On the relationship between mechanical and hydraulic apertures in rough-walled fractures. *Journal of Geophysical Research: Solid Earth*, *100*, 24629–24636.

Rice, J. R. (1968). Mathematical analysis in the mechanics of fracture. *Fracture: an advanced treatise*, *2*, 191–311.

Rice, J. R. (1972). Some remarks on elastic crack-tip stress fields. *International Journal of Solids and Structures*, *8*, 751–758.

Rubin, A. M. (1993). Tensile fracture of rock at high confining pressure: implications for dike propagation. *Journal of Geophysical Research: Solid Earth*, *98*, 15919–15935.

Rybacki, E., Reinicke, A., Meier, T., Makasi, M., & Dresen, G. (2015). What controls the mechanical properties of shale rocks?–part i: Strength and young's modulus. *Journal of Petroleum Science and Engineering*, *135*, 702–722.

Salimzadeh, S., & Khalili, N. (2015). A three-phase XFEM model for hydraulic fracturing with cohesive crack propagation. *Computers and Geotechnics*, *69*, 82–92.

Sarris, E., & Papanastasiou, P. (2011). Modeling of hydraulic fracturing in a poroelastic cohesive formation. *International Journal of Geomechanics*, *12*, 160–167.

Sarris, E., & Papanastasiou, P. (2013). Numerical modeling of fluid-driven fractures in cohesive poroelasto-plastic continuum. *International Journal for Numerical and Analytical Methods in Geomechanics*, *37*, 1822–1846.

Savitski, A., & Detournay, E. (2002). Propagation of a penny-shaped fluid-driven fracture in an impermeable rock: asymptotic solutions. *International Journal of Solids and Structures*, *39*, 6311–6337.

Schrauf, T., & Evans, D. (1986). Laboratory studies of gas flow through a single natural fracture. *Water Resources Research*, *22*, 1038–1050.

Shen, Y. (2014). A variational inequality formulation to incorporate the fluid lag in fluid-driven fracture propagation. *Computer Methods in Applied Mechanics and Engineering*, *272*, 17–33.

Shlyapobersky, J. (1985). Energy analysis of hydraulic fracturing. In *The 26^{th} US Symposium on Rock Mechanics (USRMS)* ARMA-85-0539-1. Rapid City, South Dakota: ARMA.

Shlyapobersky, J., Wong, G., & Walhaug, W. (1988). Overpressure calibrated design of hydraulic fracture stimulations. In *SPE Annual Technical Conference and Exhibition*. SPE.

Szeri, A. Z. (2010). *Fluid Film Lubrication*. Cambridge University Press.

Talon, L., Auradou, H., & Hansen, A. (2010). Permeability of self-affine aperture fields. *Physics Review E*, *82*, 046108.

Thallak, S., Holder, J., & Gray, K. (1993). The pressure dependence of apparent hydrofracture toughness. In *The 34^{th} US Symposium on Rock Mechanics (USRMS)* ARMA-93-0665. Madison, Wisconsin: ARMA.

Tsai, V., & Rice, J. R. (2010). A model for turbulent hydraulic fracture and application to crack propagation at glacier beds. *Journal of Geophysical Research - Earth Surface*, *115*, F03007.

Turon, A., Dávila, C., Camanho, P., & Costa, J. (2007). An engineering solution for mesh size effects in the simulation of delamination using cohesive zone models. *Engineering Fracture Mechanics*, *74*, 1665 – 1682.

Van Dam, D., & de Pater, C. (1999). Roughness of hydraulic fractures: The importance of in-situ stress and tip processes. In *SPE Annual Technical Conference and Exhibition* 56596. Society of Petroleum Engineers.

Vernède, S., Ponson, L., & Bouchaud, J.-P. (2015). Turbulent fracture surfaces: A footprint of damage percolation? *Physical Review Letters*, *114*, 215501.

Wang, H. (2015). Numerical modeling of non-planar hydraulic fracture propagation in brittle and ductile rocks using XFEM with cohesive zone method. *Journal of Petroleum Science and Engineering*, *135*, 127–140.

Witherspoon, P. A., Wang, J. S., Iwai, K., & Gale, J. E. (1980). Validity of cubic law for fluid flow in a deformable rock fracture. *Water Resources Research*, *16*, 1016–1024.

Xing, P., Yoshioka, K., Adachi, J., El-Fayoumi, A., & Bunger, A. P. (2017). Laboratory measurement of tip and global behavior for zero-toughness hydraulic fractures with circular and blade-shaped (PKN) geometry. *Journal of the Mechanics and Physics of Solids*, *104*, 172–186.

Yao, Y., Liu, L., & Keer, L. M. (2015). Pore pressure cohesive zone modeling of hydraulic fracture in quasi-brittle rocks. *Mechanics of Materials*, *83*, 17–29.

Zhang, X., Jeffrey, R., & Detournay, E. (2005). Propagation of a hydraulic fracture parallel to a free surface. *International Journal for Numerical and Analytical Methods in Geomechanics*, *29*, 1317–1340.

Zhang, Z., Nemcik, J., Qiao, Q., & Geng, X. (2015). A model for water flow through rock fractures based on friction factor. *Rock Mechanics and Rock Engineering*, *48*, 559–571.

Zia, H., & Lecampion, B. (2017). Propagation of a height contained hydraulic fracture in turbulent flow regimes. *International Journal of Solids and Structures*, *110*, 265–278.

Zimmerman, R. W., & Bodvarsson, G. S. (1996). Hydraulic conductivity of rock fractures. *Transport in Porous Media*, *23*, 1–30.

Supplementary materials for "Propagation of a plane-strain hydraulic fracture accounting for a rough cohesive zone"

Dong Liu[a], Brice Lecampion[a,]

[a] *Geo-Energy Laboratory-Gaznat Chair on Geo-Energy, Ecole Polytechique Fédérale de Lausanne, EPFL-ENAC-IIC-GEL, Lausanne CH-1015, Switzerland*

1. Energy balance

Following Lecampion & Detournay (2007), we write the energy balance of a propagating cohesive HF by combining the energy dissipation in the fluid and solid. The external power provided by injecting fluid at a flow rate Q_o, under the inlet pressure $p_f(x=0,t)$, is balanced by the rate of work expended by the fluid on the walls of the fracture and by viscous dissipation. Hence,

$$Q_o p_f(x=0,t) = 2\int_0^{\ell_f} p_f \frac{\partial w}{\partial t}\mathrm{d}x - 2\int_0^{\ell_f} q\frac{\partial p}{\partial x}\mathrm{d}x, \quad q = -\frac{w^3}{\mu' f}\frac{\partial p}{\partial x} \tag{1}$$

where the cavity pressure in the lag zone is neglected in the above expression. By differentiating the global continuity equation with time,

$$Q_o = 2\int_0^{\ell_f} \frac{\partial w}{\partial t}\mathrm{d}x + 2\dot{\ell}_f w(\ell_f) \tag{2}$$

After multiplying the above expression by σ_o and subtracting it from Eq. (1), we obtain an alternative form of the energy balance in the fluid,

$$Q_o p_{f0} = Q_o\sigma_o + 2\int_0^{\ell_f} p\frac{\partial w}{\partial t}\mathrm{d}x - 2\int_0^{\ell_f} q\frac{\partial p}{\partial x}\mathrm{d}x - 2\sigma_o\dot{\ell}_f w(\ell_f) \tag{3}$$

For a fracture propagating quasi-statically in limit equilibrium in the solid, the fracture energy release rate is then written as the decrease of the strain energy rate and the work rate of the external forces (Keating & Sinclair, 1996).

$$\int_0^{\ell_f} p\frac{\partial w}{\partial t}\mathrm{d}x - \int_0^{\ell_f} w\frac{\partial p}{\partial t}\mathrm{d}x - \int_{\ell_f}^{\ell} \sigma_o\frac{\partial w}{\partial t}\mathrm{d}x + \int_0^{\ell} \sigma_{coh}\frac{\partial w}{\partial t}\mathrm{d}x - \int_0^{\ell} w\frac{\partial \sigma_{coh}}{\partial t}\mathrm{d}x = 0 \tag{4}$$

Eqs. (3) and (4) can be combined to yield an energy balance for the whole system.

$$P_e = Q_o p_{f0} = \dot{W}_o + \dot{W}_e + \dot{W}_l + D_k + D_v \tag{5}$$

where

$$\begin{aligned}
\dot{W}_o &= Q_o \sigma_o, \\
\dot{W}_e &= \int_0^{\ell_f} p \frac{\partial w}{\partial t} \mathrm{d}x + \int_0^{\ell_f} w \frac{\partial p}{\partial t} \mathrm{d}x - \sigma_o \int_{\ell_f}^{\ell} \frac{\partial w}{\partial t} \mathrm{d}x, \\
\dot{W}_l &= 2 \int_{\ell_f}^{\ell} \sigma_o \frac{\partial w}{\partial t} \mathrm{d}x - 2\sigma_o \dot{\ell}_f w(\ell_f) = 2\sigma_o \frac{\mathrm{d}}{\mathrm{d}t} \int_{\ell_f}^{\ell} w \mathrm{d}x, \\
D_k &= -\int_0^{\ell} w \frac{\partial \sigma_{coh}}{\partial t} \mathrm{d}x + \int_0^{\ell} \sigma_{coh} \frac{\partial w}{\partial t} \mathrm{d}x \\
D_v &= -2 \int_0^{\ell_f} q \frac{\partial p}{\partial x} \mathrm{d}x
\end{aligned} \tag{6}$$

Using the linear-softening cohesive traction-separation law, we rewrite D_k in the coordinates of a moving tip

$$D_k = \int_{\ell-\ell_{coh}}^{\ell} \sigma_c \frac{w}{w_c} \frac{\partial w}{\partial t} \mathrm{d}x + \int_{\ell-\ell_{coh}}^{\ell} \sigma_c \left(1 - \frac{w}{w_c}\right) \frac{\partial w}{\partial t} \mathrm{d}x = \sigma_c \int_{\ell-\ell_{coh}}^{\ell} \frac{\partial w}{\partial t} \mathrm{d}x = \sigma_c \int_0^{\ell_{coh}} \frac{\partial w}{\partial t} \mathrm{d}\hat{x} \tag{7}$$

where

$$\hat{x} = \ell - x, \quad \frac{\partial w}{\partial t} = \left.\frac{\partial w}{\partial t}\right|_{\hat{x}} - (-\dot{\ell}) \frac{\partial w}{\partial \hat{x}} \tag{8}$$

The energy dissipation during the fracturing process D_k can be thus simplified as follows

$$D_k = \sigma_c \int_0^{\ell_{coh}} \left.\frac{\partial w}{\partial t}\right|_{\hat{x}} \mathrm{d}\hat{x} + \sigma_c \dot{\ell} \int_0^{\ell_{coh}} \frac{\partial w}{\partial \hat{x}} \mathrm{d}\hat{x} = \sigma_c \int_0^{\ell_{coh}} \left.\frac{\partial w}{\partial t}\right|_{\hat{x}} \mathrm{d}\hat{x} + 2\dot{\ell}\left(\frac{1}{2}\sigma_c w(\hat{x} = \ell_{coh})\right) \tag{9}$$

2. Complementary results for a smooth cohesive hydraulic fracture with $\mathcal{K}_m = 0.495$

We show the time evolution of the cohesive zone length, the ratio between the lag and cohesive zone sizes, the apparent fracture energy, and the ratio of the energies dissipated in fluid viscous flow and in the creation of new fracture surfaces in Fig. 1 as complimentary information of Fig. 7 in the main text.

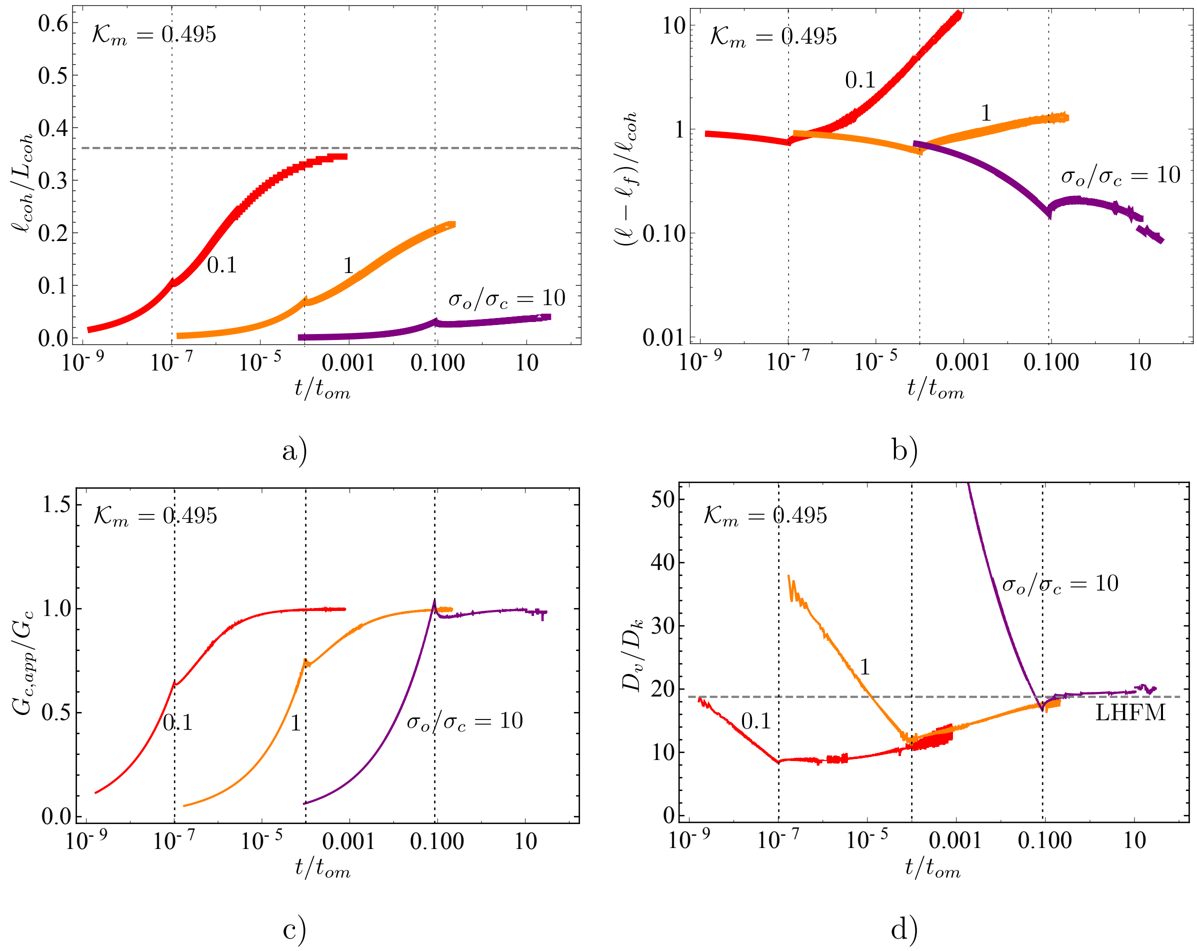

Figure 1: $\mathcal{K}_m = 0.495$: evolution of a) the cohesive zone length ℓ_{coh}/L_{coh}, b) the ratio between the lag and cohesive zone sizes $(\ell - \ell_f)/\ell_{coh}$, c) the apparent fracture energy $G_{c,app}/G_c$, and d) the ratio of the energies dissipated in fluid viscous flow and in the creation of new fracture surfaces D_v/D_k with t/t_{om}. The red, orange and purple curves indicate the smooth cohesive hydraulic fracture with the confining stress $\sigma_o/\sigma_c = 0.1, 1, 10$ with the dotted vertical lines as their corresponding cohesive zone nucleation period. The dashed horizontal line in Figure a) represents the small-scale yielding asymptote ($\approx 0.115\pi$) of the cohesive zone length for the linear-softening cohesive model (Dempsey et al., 2010). The dashed horizontal line in Figure d) represents the LHFM limit with zero lag.

3. Tip asymptote comparison with solutions for a semi-infinite cohesive hydraulic fracture

When the cohesive fraction is very small in a smooth HF, the tip asymptote tends to converge to the semi-infinite cohesive hydraulic fracture solution as reported in Garagash (2019). We show this trend in Fig. 2 for $\sigma_o/\sigma_c = 0.1, 1$ with different values of the cohesive-to-lag fracture energy ratio Γ_c which is defined as

$$\Gamma_c = \frac{G_c}{G_o} = \frac{G_c}{w_o\sigma_o} = \frac{1}{2}\frac{w_c\sigma_c\sigma_o}{E'\mu'V} \tag{10}$$

$$w_o = \frac{\sigma_o}{E'}\ell_o, \quad \ell_o = \frac{\mu'V}{E'}\left(\frac{E'}{\sigma_o}\right)^3 \tag{11}$$

where V represents the fracture front velocity and ℓ_o the lag length scale (Garagash, 2019). The fracture opening in Fig. 2 is normalized by the far field 'm' asymptote:

$$w_\infty = 2^{1/3}3^{5/6}\left(\frac{\mu'V}{E'}\right)^{1/3}(\ell - x)^{2/3} \tag{12}$$

The tip asympotote of a finte fracture shows an offset from the semi-infinite solution (Fig. 2). This offset results from the finite size of the fracture dimension and a relatively important fraction of the cohesive zone (see Table. 1).

References

Dempsey, J. P., Tan, L., & Wang, S. (2010). An isolated cohesive crack in tension. *Continuum Mechanics and Thermodynamics*, *22*, 617–634.

Garagash, D. I. (2019). Cohesive-zone effects in hydraulic fracture propagation. *Journal of the Mechanics and Physics of Solids*, *133*, 103727.

$\Gamma_c = G_c/G_o$ Color in Fig. 2	$10^{-5/2}$ Cyan	0.01 Magenta	$10^{-3/2}$ Pink	0.1 Red	$10^{-1/2}$ Orange	1 Purple	$10^{1/2}$ Black	10 Blue	$10^{3/2}$ Gray
ℓ_{coh}/ℓ ($\sigma_o/\sigma_c = 0.1$) (%)	5.0	33.7	6.90	44.0	5.57	11.5	11.4		
ℓ_{coh}/ℓ ($\sigma_o/\sigma_c = 1$) (%)		26.2	4.9	22.9	3.50	39.2	3.50	11.1	10.9

Table 1: Cohesive fractions of finite fractures in Fig. 2.

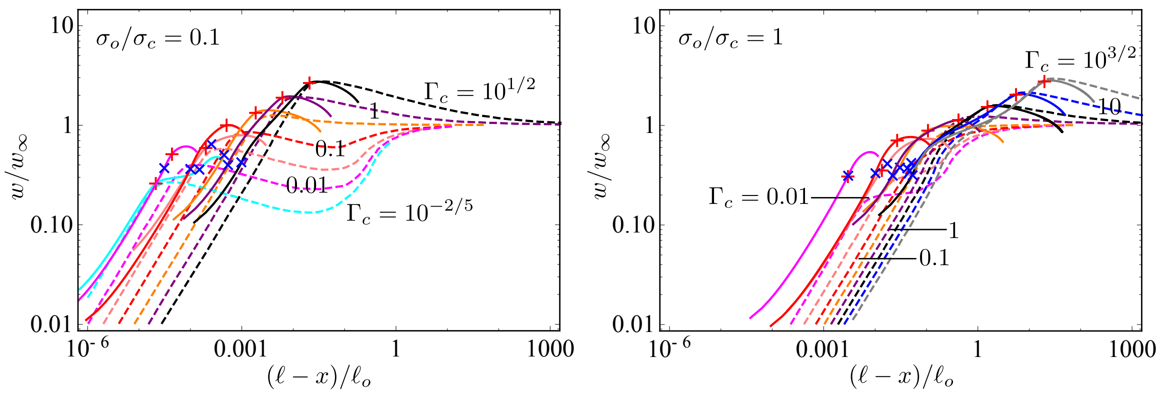

Figure 2: The crack opening normalized by the far-field 'm'-asymptote for $\sigma_o/\sigma_c = 0.1, 1$ and various values of $\Gamma_c = G_c/G_o$ (see the definition in Eq. (10)) between $10^{-5/2}$ and $10^{3/2}$ in $10^{1/2}$ increments on the logarithm scale. The dashed curves are semi-infinite solutions in Garagash (2019). The solid curves are results of a smooth plane-strain cohesive hydraulic fracture whose corresponding cohesive fractions are shown in Table. 1. "+" indicates the boundary of the cohesive zone and "×" the fluid front location.

Keating, R., & Sinclair, G. (1996). On the fundamental energy argument of elastic fracture mechanics. *International Journal of Fracture*, *74*, 43–61.

Lecampion, B., & Detournay, E. (2007). An implicit algorithm for the propagation of a hydraulic fracture with a fluid lag. *Computer Methods in Applied Mechanics and Engineering*, *196*, 4863–4880.